Contributions to Mineralogy and Petrology (2022) 177:23
https://doi.org/10.1007/s00410-022-01890-0

ORIGINAL PAPER

Apatite chemistry as a petrogenetic–metallogenic indicator for skarn ore-related granitoids: an example from the Daye Fe–Cu–(Au–Mo–W) district, Eastern China

Run-Jie Zhou[1] · Guang Wen[1] · Jian-Wei Li[1] · Shao-Yong Jiang[1,2] · Hao Hu[1] · Xiao-Dong Deng[1] · Xin-Fu Zhao[1] · Dai-Rong Yan[3] · Ke-Tao Wei[4,5] · Heng-An Cai[4] · Shi-Chao Shang[4] · Bai-Cun Li[4] · Xu-Ke Dai[6]

Received: 4 September 2021 / Accepted: 9 January 2022 / Published online: 31 January 2022

Abstract

The Daye district represents one of the largest concentrations of skarn deposits in eastern China. There are two major types of skarn deposits (Fe skarn vs. Cu skarn) within this district, both genetically related to late Mesozoic high-K calc-alkaline granitoids. In this study, we present in situ compositional and Sr–Nd isotopic investigations of apatite from granitoids associated with Fe skarn and Cu skarn deposits to put constraints on the magma source, evolution, and volatile composition, which provide significant new insights into the genesis of the two contrasting mineralization styles in the Daye district. Apatite from granitoids related to Cu skarns and Lingxiang Fe skarn has $\varepsilon_{\mathrm{Nd}}(t)$ values of -8 to -4, similar to that of the contemporaneous mafic rocks in the Daye district, which were dominantly derived from an enriched lithospheric mantle source. Apatite in granitoids associated with the Chengchao Fe skarn has lower $\varepsilon_{\mathrm{Nd}}(t)$ values of -15 to -9, suggesting larger degrees of contaminations from ancient lower crust materials. Fractionation models based on apatite Sr/Y and Eu/Eu* ratios, suggest that magmas related with the Cu skarns have experienced amphibole-dominated fractionation under high pressure and hydrous conditions, whereas those associated with Fe skarns have undergone plagioclase-dominated fractionation at relatively low pressure and dry conditions. Based on results of apatite compositional analysis and apatite-melt partitioning data, the estimated magma Cl contents for the Fe skarn range from 3260 to 13,940 ppm, significantly higher than those for the Cu skarn (Cl = 430–5990 ppm). Apatite from Fe skarn-related intrusions has $(^{87}\mathrm{Sr}/^{86}\mathrm{Sr})_t$ ranging from 0.7073 to 0.7082, whereas the variety from Cu skarn-related intrusions displays lower $(^{87}\mathrm{Sr}/^{86}\mathrm{Sr})_t$ of 0.7054–0.7061. These Sr isotope data, combined with whole-rock S isotopes of this study and previous investigations suggest that the Fe skarn-related intrusions have assimilated larger amount of evaporite-bearing carbonate during magma ascent and emplacement. The assimilation process may have not only promoted magmatic water exsolution but also provided sufficient amount of Cl^- and SO_4^{2-}, which facilitated effective complexation and transportation of Fe^{2+} and subsequent oxidization of ferrous Fe to precipitate magnetite, respectively. We suggest that evaporite assimilation into the granitoid magmas has played a crucial role in the large-scaled Fe skarn mineralization in the Daye district. This study highlights that apatite is a sensitive petrogenetic-metallogenic indicator for granitoids and thus can be useful in mineral exploration.

Keywords Apatite geochemistry · Skarn deposit · Granitoid metallogeny · Magmatic process · Daye district

---

Communicated by Hans Keppler.

✉ Guang Wen
guangwen@cug.edu.cn

✉ Jian-Wei Li
jwli@cug.edu.cn

[1] State Key Laboratory of Geological Processes and Mineral Resources and School of Earth Resources, China University of Geosciences, Wuhan 430074, China

[2] Collaborative Innovation Centre for Exploration of Strategic Mineral Resources, China University of Geosciences, Wuhan 430074, China

[3] School of Resources and Environmental Engineering, Wuhan University of Technology, Wuhan 430074, China

[4] The First Geological Brigade of Hubei Geological Bureau, Daye 435100, China

[5] Hubei Provincial Key Laboratory of Resource and Eco-Geological Environment, Hubei Geological Bureau, Wuhan 430022, China

[6] The Seventh Geological Brigade of Hubei Geological Bureau, Yichang 443000, China

Introduction

Apatite [$Ca_5(PO_4)_3(F, OH, Cl)$] is a ubiquitous accessory mineral in magmatic rocks (Belousova et al. 2002; Bruand et al. 2014). It is an important host for rare-earth elements (REEs) and contains relatively high concentration of Sr, Y, Th, and U (Sha and Chappell 1999; Prowatke and Klemme 2006; Xiao et al. 2021). The trace element compositions of apatite are sensitive to physicochemical parameters of magmas such as temperature, oxygen fugacity, water content, and melt composition (Bruand et al. 2016; Konecke et al. 2017; Li and Costa 2020), and, therefore, can be a useful tool in petrogenetic studies of magmatic rocks. Apatite also incorporates significant amounts of volatile elements and can be used to investigate the F, Cl, and S budgets of magmas, which are crucial in the formation of magmatic-hydrothermal ore systems (Streck and Dilles 1998; Parat et al. 2011; Duan and Jiang 2018; Sun et al. 2019; Duan et al. 2021). Over the past decade, there has been increased interest in apatite geochemistry applied to petrogenetic and metallogenic problems of porphyry Cu–Au(–Mo) systems (Streck and Dilles 1998; Xing et al. 2019; Cao et al. 2022). To date, few studies have been undertaken to use apatite

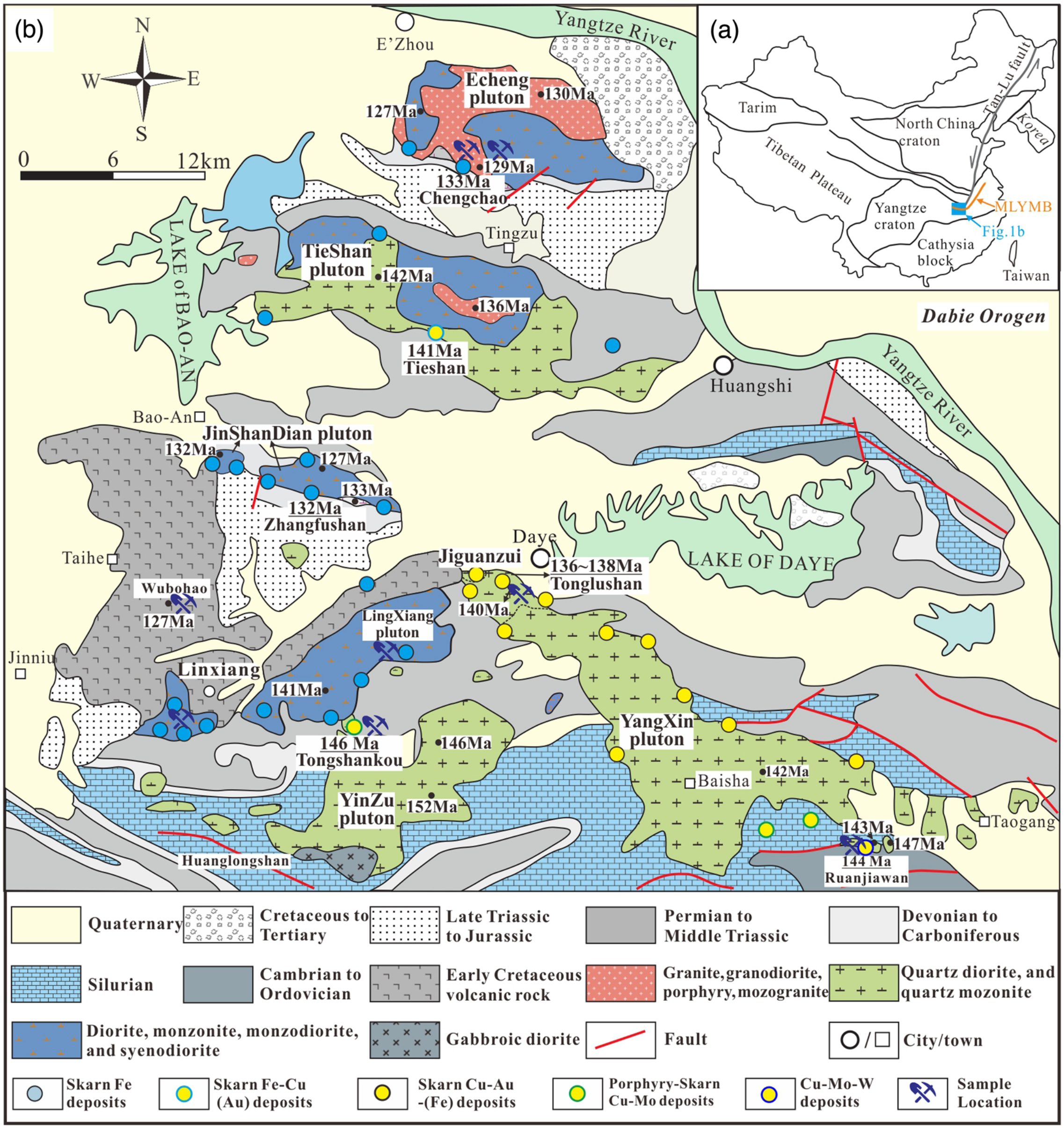

Fig. 1 Geological map showing the distribution of skarn deposits and ages of the major intrusions in the Daye district (modified from Shu et al. 1992; the intrusion ages are from Li et al. (2008, 2009, 2010a, b) and Xie et al. (2011a, b))

geochemistry to better understand the genetic link between granitoid intrusions and skarn systems, which are mined for a large variety of metals such as Fe, Cu, Pb, Zn, W, Mo, Au, and Sn.

The Daye ore district, located in eastern China, hosts more than 50 skarn deposits (Fig. 1) that are genetically associated with intrusive rocks ranging in composition from gabbroic diorite to granite intruding late Paleozoic to early Triassic marine carbonates and clastic rocks (Shu et al. 1992). Iron-only skarns and Cu-rich polymetallic skarns are the two major types of mineralization in this district, hereafter termed as Fe skarn and Cu skarn, respectively. The Fe skarns are primarily related to diorite with magnetite being the only recoverable commodity, whereas Cu skarns are associated with granodiorite and quartz diorite and variably contain appreciable Au, Mo, Fe, W of economic significance (Li et al. 2008, 2010a, 2014a; Xie et al. 2015; Deng et al. 2015). Previous whole-rock Sr–Nd isotopic studies suggest that the granitoids associated with Fe skarns and Cu skarns are largely derived from an enriched mantle source with variable degrees of crustal contamination (Li et al. 2009; Li et al. 2013a; Xie et al. 2015; Chu et al. 2020; Zhang et al. 2021). More recently, a zircon geochemistry study shows that the granitoids associated with Cu skarns are generally more oxidized and more hydrous than those associated with Fe skarns (Wen et al. 2020a). However, few constraints have been placed on the petrological processes and volatile compositions of the ore-related granitoids, limiting the understanding of the major controls of the contrasting skarn mineralization styles (Fe vs. Cu skarn) in the Daye district.

In this paper, we present in situ compositional data and Sr–Nd isotopes of apatite from granitoid intrusions associated with two Fe skarn (Chengchao and Lingxiang) and three Cu skarn deposits (Tongshankou, Tonglushan, and Ruanjiawan) to constrain the magma source, evolution, and volatile compositions. The main objective of this study was to reveal the possible major controls of magmatic processes on the two distinct skarn mineralization styles in the Daye district. We demonstrate that apatite chemistry is a sensitive indicator for petrogenetic-metallogenic processes and can be useful in ore exploration.

Geological background

The Daye ore district located in the westernmost part of the Middle-Lower Yangtze River Valley metallogenic belt (MLYMB) (Li et al. 2009; Fig. 1a). Stratigraphic units in Daye ore district mainly consist of Cambrian to Middle Triassic marine carbonate and clastic rocks, late Triassic to Cenozoic continental sedimentary rocks and Cretaceous terrestrial volcanic assemblages (Fig. 1b). Most of the skarn deposits in the district are hosted by the Triassic carbonate rocks (Fig. 1b). The Triassic strata can be divided, from the base upward, into the Daye, Jialingjiang, and Puqi Formations (Fms.; Fig. 2). The 200–1600 m thick Daye Fm. is composed of shales and limestones in its lower member, dolostones, dolomitic limestones, and minor interbedded evaporites in the middle member and dolostones in the upper member. The Jialingjiang Fm., with a total thickness of 20–400 m, is dominated by dolomitic limestones with many intercalations of evaporites and host numerous economic gypsum deposits and Sr deposits (Shu et al. 1992; Zeng et al. 2020). Dissolution breccias and sulfate-rich evaporites are widespread in the Jialingjiang Formation (Shu et al. 1992). The Puqi Fm. consists of 450–1000 m of purple silty claystone and clay siltstone (Fig. 2). Early Cretaceous volcanism resulted in more than 2000 m of volcanic associations consisting of basalt, basaltic andesite, trachyandesite, trachydacite, and rhyolite in the Jinniu volcanic basin at the western part of the region (Xie et al. 2011a). From the base to the top, these volcanic associations are composed of Majiashan, Lingxiang, and Dasi Formations. SHRIMP zircon U–Pb dating of the volcanic rocks yielded weighted mean ^{206}Pb/^{208}U age from 130 to 125 Ma (Xie et al. 2011a). These volcanic rocks were formed contemporaneously with the Chengchao Fe skarn deposits with age of 132–128 Ma (Xie et al. 2012; Hu et al. 2017). The zircon Hf isotope and whole-rock Sr–Nd–Pb isotope of the basalts in the Jinniu basin are similar with those of the early Cretaceous basalts in other volcanic basins from the MLYMB, which were derived from an enriched lithospheric mantle (Xie et al. 2011a, b).

The Daye region contains six major granitoid plutons emplacing into the Devonian to early Triassic sedimentary rocks (Fig. 1b). These include, from north to south, Echeng complex consisting of diorite, quartz monzonite and granite, Tieshan complex consisting of quartz diorite and a small volume of gabbro-diorite, Jinshandian diorite, Lingxiang diorite, Yinzu and Yangxin complex consisting of granodiorite, quartz diorite, and gabbro-diorite (Fig. 1b). In addition, there are numerous granodiorite stocks and dikes surrounding or intruding the major plutons. Recent geochronological studies have identified two episodes of magmatism (Li et al. 2009; Xie et al. 2011b; Hu et al. 2020). The first episode (ca.150–136 Ma) is represented by plutonic magmatism of granodiorite and quartz diorite, which are associated with more than 30 Cu skarns. The second episode (ca. 133–127 Ma) mainly formed diorite and quartz monzonite intrusions that are in association with more than 10 Fe skarns (Fig. 1b). Iron oxide-apatite mineralization was recently identified in Wangbaoshan Fe skarn deposit in the Jinniu volcanic basin

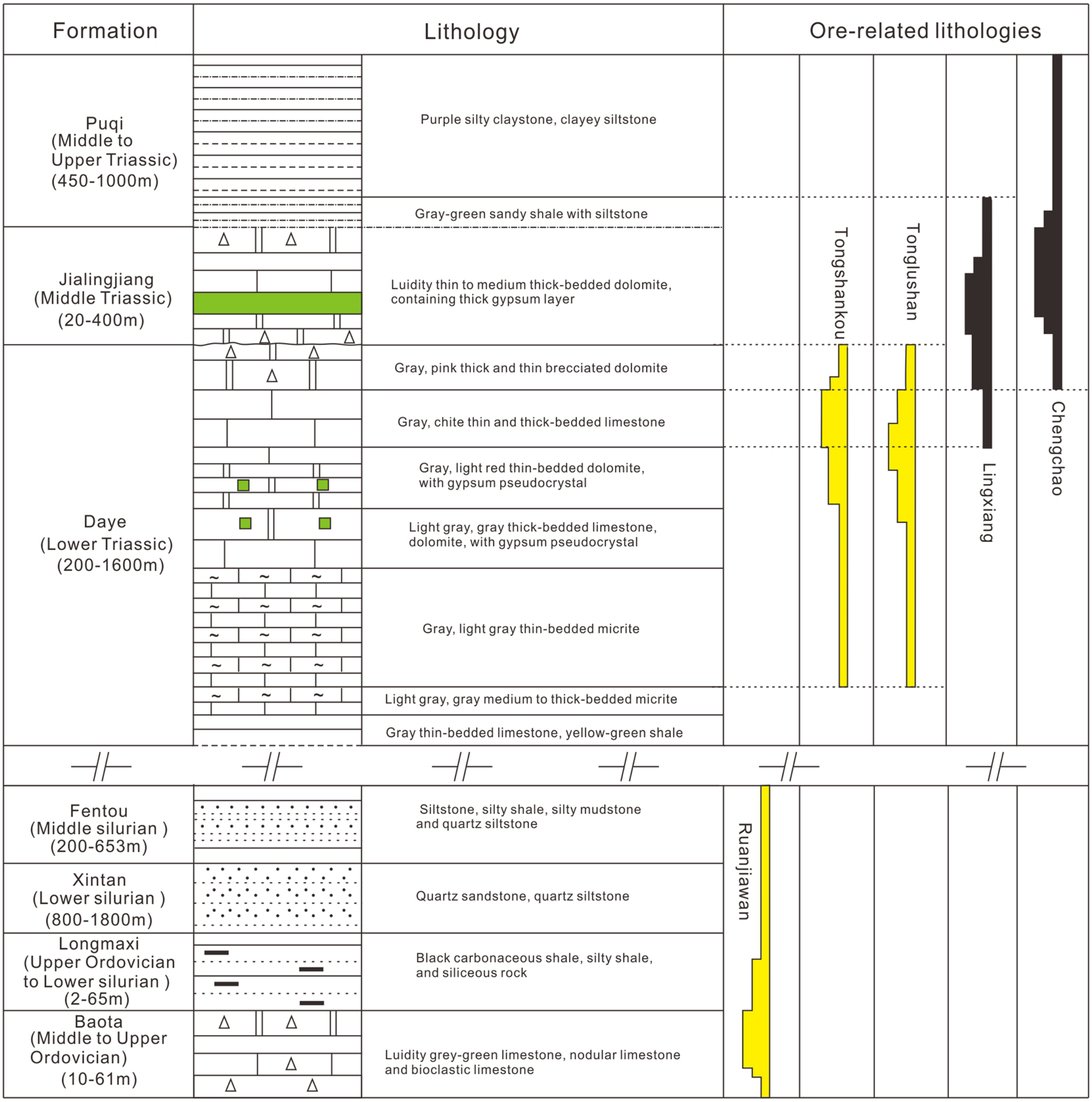

Fig. 2 Stratigraphic column of the Daye district showing marine sedimentary rocks into which the ore-related intrusions emplaced. The green band and square represent the gypsum layer and gypsum pseudocrystal, respectively. Note that the intrusions associated with the two Fe skarn deposits investigated in this study are emplaced into the Jialingjiang Formation that contains abundant evaporites (modified from Shu et al. 1992; Xie et al. 2020)

(Hu et al. 2020). It is genetically associated with subvolcanic diorite porphyries beneath the skarn ores, with ore-related titanite and apatite U–Pb ages of 132.5 ± 2.4 Ma and 128.4 ± 3.0 Ma, respectively (Hu et al. 2020).

Geology of the ore deposits

Five deposits including three Cu skarn deposits (Tongshankou, Ruanjiawan, Tonglushan) and two Fe skarn deposits (Lingxiang, Chengchao) are investigated in this study (Fig. 1). The major geological characteristics of these Cu and Fe skarn deposits have been described by previous studies (e.g., Li et al. 2008, 2010a, 2014a, 2019; Deng et al. 2015) and are briefly described below.

Tongshankou skarn Cu–Mo deposit

The Tongshankou deposit is situated in the south part of the Daye district (Fig.1) and has proven reserves of 0.52 Mt Cu at a grade of 0.9–1.0 wt% and 2000 t Mo at a grade of 0.02–0.07 wt% (Li et al. 2008). Roughly east-northeast and northwest-striking faults are well developed, which have facilitated emplacement of the ore-related Tongshankou granodiorite stock and localization of the ore bodies (Li et al. 2008). The Cu mineralization is dominantly distributed along the contact between the Tongshankou granodiorite and the Lower Triassic Daye Formation, whereas the Mo mineralization occurs within the granodiorite (Shu et al. 1992; Li et al. 2008). Appreciable W mineralization (scheelite) was recently found in the skarn assemblage in the contact zone in this deposit (Han et al. 2020). The ore-related granodiorites have porphyritic texture and are rich in phenocrysts consisting of plagioclase (30–50 vol%), K-feldspar (10–15 vol%), quartz (15–20 vol%), amphibole (10–15 vol%), biotite (~5 vol%) (Fig. 3a–c) with the groundmass of quartz, plagioclase, and biotite (Fig. 3b, c). The accessory minerals include apatite, zircon, titanite, and magnetite (Fig. 3b, c).

Tongshankou deposit has abundant skarn with exoskarn volumetrically more significant than endoskarn. The exoskarn consists of prograde skarn and retrograde skarn assemblages (Shu et al. 1992; Li et al. 2008). The former mainly comprises garnet, diopside, and K-feldspar with minor titanite and is locally overprinted by the retrograde skarn assemblage consisting of epidote, actinolite, phlogopite, chlorite, fluorite, and quartz. The endoskarn consists mainly of garnet with minor diopside and epidote that occurs as irregular veins typical of a few centimeters

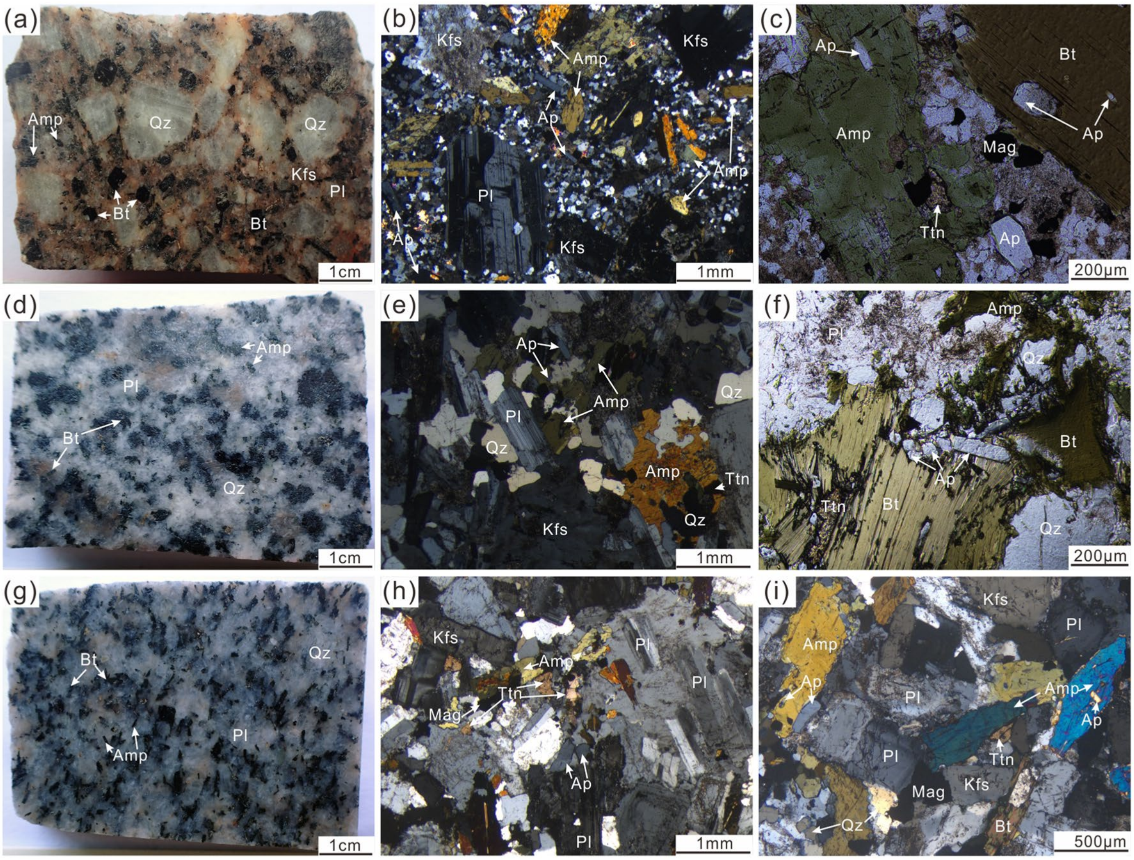

Fig. 3 Hand specimens and photomicrographs of igneous rocks associated with Cu skarn. **a**–**c** for Tongshankou granodiorite, **d**–**f** for Ruanjiawan quartz diorite and **g**, **h** for Tonglushan quartz diorite. **a** Granodiorite mainly composed of K-feldspar, plagioclase, amphibole, biotite, and quartz. **b, c** Granodiorite porphyry with plagioclase, K-feldspar, and amphibole as phenocrysts and quartz as groundmass. **d**, **e** Quartz diorite composed of amphibole, plagioclase, biotite, and quartz. **f** Euhedral apatite grains coexisting with anhedral amphibole and subhedral-anhedral biotite. **g** Quartz diorite mainly composed of amphibole, plagioclase, biotite, and quartz. **h** Prismatic apatite coexisting with euhedral K-feldspar and plagioclase. **i** Columnar apatite occurring as inclusions in euhedral amphibole. *Amp* amphibole, *Ap* apatite, *Bt* biotite, *Kfs* K-feldspar, *Mag* magnetite, *Pl* plagioclase, *Qz* quartz, *Ttn* Titanite

within the Tongshankou granodiorite. The metallic minerals, such as magnetite, molybdenite, pyrite, bornite, and chalcopyrite, are mainly associated with the retrograde skarn assemblage. The phlogopite ^{40}Ar/^{39}Ar plateau dating and molybdenite Re–Os isochron dating from previous studies indicate the Tongshankou deposit was formed at ca. 143 Ma (Li et al. 2008).

Ruanjiawan W–Cu–Mo skarn deposit

The Ruanjiawan W–Cu–Mo deposit, containing of 23,356 t WO_3, 17,320 t Cu, and 2439 t Mo, is situated in the south-eastern part of Daye (Fig. 1b; Shu et al. 1992; Deng et al. 2015). The deposit comprises three major ore bodies, the geometries of which are controlled by East–West trending faults (Deng et al. 2015). The No. I ore body is the most significant one accounting for 60% of the total W reserves of the deposit. The No. III ore body is dominated by ores of Cu and Mo without W (Shu et al. 1992; Deng et al. 2015). The mineralization is related to a quartz diorite stock that intrudes Ordovician carbonates and Silurian clastic rocks (Fig. 2). The Ruanjiawan quartz diorite stock is located in the south-eastern portion of the Yangxin complex intrusion (Fig. 1b). The stock is in lentoid shape occupying an area of about 1.286 km^2 with length of 3450 m and width of 80–670 m. The quartz diorite is medium to coarse-grained and composed of plagioclase (50–60 vol%), quartz (10–15 vol%), amphibole (5–10 vol%), and biotite (5–10 vol%) (Fig. 3d–f), with apatite, titanite, zircon, and magnetite as accessory phases (Fig. 3e, f).

Exoskarn is massive in this deposit, which is dominated by a prograde skarn assemblage consisting of garnet, diopside, and K-feldspar with minor titanite. The retrograde skarn composed of phlogopite, actinolite, epidote, chlorite, and quartz locally replace the prograde skarn. Endoskarn consisting of garnet with minor diopside commonly occurs as irregular veins within the quartz diorite. Massive garnet endoskarn is locally observed at the intrusive contact. Scheelite, chalcopyrite, and molybdenite are the dominant ore minerals. Dating of hydrothermal titanite from skarn ore yields U–Pb age of 142 ± 2 Ma (Deng et al. 2015), in agreement with molybdenite Re–Os isochron age of 143.6 ± 1.7 Ma (Xie et al. 2007), which are consistent with the zircon U–Pb age of 144 ± 1 Ma for the ore-related quartz diorite (Deng et al. 2015).

Tonglushan Cu–Au–Fe skarn deposit

The Tonglushan Cu–Au–Fe deposit, containing 1.34 Mt Cu @ 1.78 wt%, 83 t Au @ 0.38 g/t, and 65 Mt Fe @ 41% wt%, is located in the central part of the Daye district (Li et al. 2010a). There are three major Cu–Au–Fe ore zones in this deposit. The most important ore zone extends NNE-SSW and consists of eight ore bodies. The mineralization mainly distributes along the contact between the quartz diorite stock and dolomitic limestones of the Lower Triassic Daye Formation (Fig. 2). The Tonglushan quartz diorite stock is 4 km long and 3.5 km wide with an area of about 11 km^2, which is located in the north-western portion of the Yangxin intrusive complex. The quartz diorite is grey-white in color and medium to coarse grained (Fig. 3g–i). It contains plagioclase (50–60 vol%), K-feldspar (10–20 vol%), quartz (5–10 vol%), amphibole (5–10 vol%), and biotite (~ 5 vol%), with accessory apatite, magnetite, titanite, and zircon (Fig. 3h, i).

The Tonglushan deposit is characterized by extreme development of massive exoskarn that is composed of prograde and retrograde assemblages. The prograde assemblage mainly consists of garnet, diopside, and wollastonite which is variably replaced by retrograde actinolite, epidote, phlogopite, and chlorite. Endoskarn consisting of diopside, garnet, and epidote is abundant in the quartz diorite. Massive endoskarn is observed near the intrusive contact. Ore minerals comprise dominantly magnetite, chalcopyrite, bornite, and hematite, followed by chalcocite, azurite, molybdenite, pyrite, and native gold and gangue minerals are dominated by garnet, diopside, phlogopite, actinolite, chlorite, quartz, and calcite. SIMS and LA-ICP-MS zircon U–Pb dating yield reproducible age of 139.8 ± 0.9 Ma and 138.8 ± 1.9 Ma (Li et al. 2010a; Wen et al. 2020a), respectively, for the Tonglushan quartz diorite. LA-ICP-MS U–Pb dating of hydrothermal titanite in the skarn ore yields age of 135.9 ± 1.3 Ma (Li et al. 2010a), which approximates to the zircon U–Pb age of the quartz diorite.

Lingxiang Fe skarn deposit

The Lingxiang Fe deposit is situated in the southwestern part of the Daye region, with reserves of 49 Mt ores grading 25–65 wt%. The ore bodies are located in the contact between carbonate xenoliths of Middle Triassic Jialingjiang Formation and the diorite intrusion (Shu et al. 1992). The diorite is fine to medium-grained, consisting of amphibole (15–20 vol%), plagioclase (25–30 vol%), and biotite (5–10 vol%) (Fig. 4a–c) together with accessories of magnetite, zircon, apatite, and titanite (Fig. 4b, c).

The Lingxiang deposit consists of three ore segments and they have approximately isometric distribution. Iron orebodies in the deposit appear as irregular columnar, saddle or lenticular shapes. Exoskarn is massive in this deposit, consisting of diopside with minor garnet, phlogopite, actinolite, and chlorite. Endoskarn consisting of diopside, epidote, and chlorite occurs mostly as disseminations and veins that are widespread in the diorite. Magnetite is the dominant ore mineral and hematite; limonite and pyrite are locally abundant. SIMS and LA-ICP-MS zircon U–Pb dating yield ages

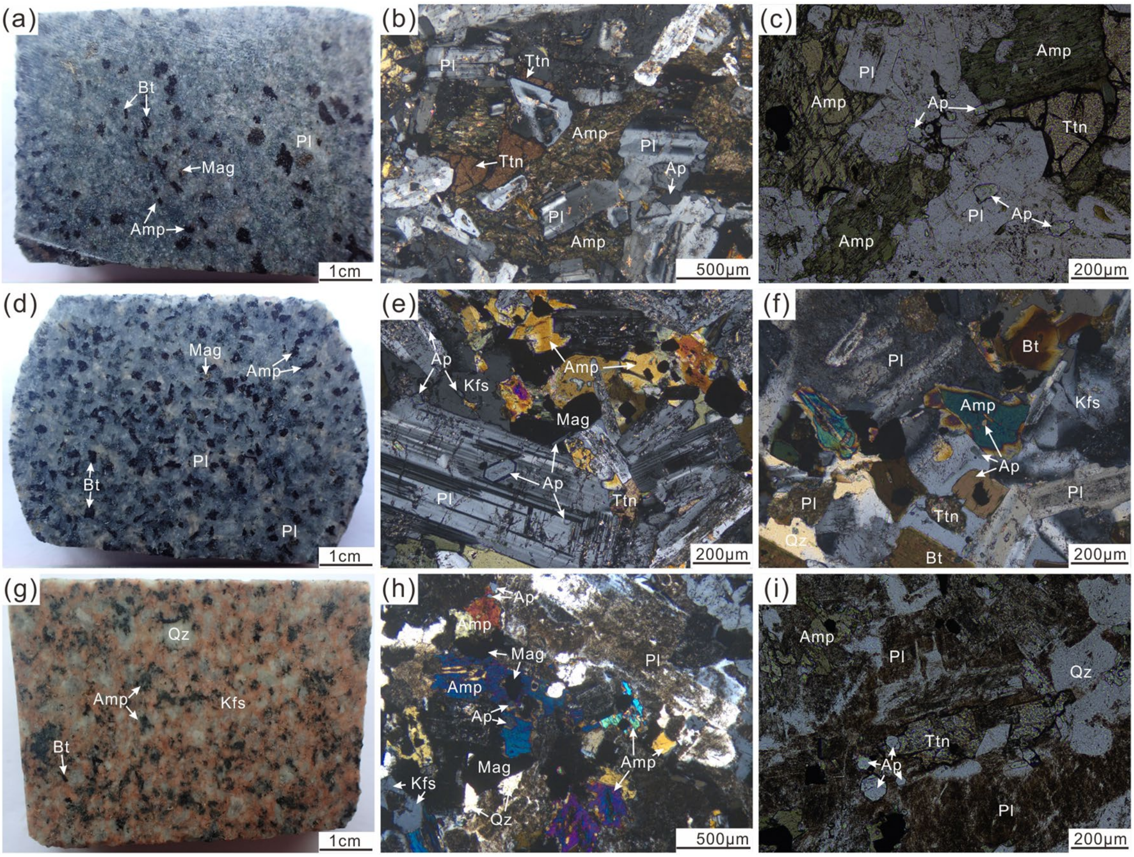

Fig. 4 Hand specimens and photomicrographs of igneous rocks associated with Fe skarn. **a**–**c** for Lingxiang diorite, **d**–**f** for Chengchao diorite and **g**, **h** for Chengchao quartz monzonite. **a** Fresh diorite mainly composed of plagioclase, amphibole, and biotite. **b** Euhedral plagioclase coexisting with subhedral–anhedral amphibole define the major mineral assemblages. **c** Euhedral subhedral amphibole coexisting with columnar apatite. **d** Diorite predominantly composed of amphibole, plagioclase, and biotite. **e**, **f** Columnar apatite occurring as inclusions in euhedral plagioclase, subhedral–anhedral amphibole, and biotite. **g** Quartz monzonite mainly composed of K-feldspar, plagioclase, and quartz. **h**, **i** Prismatic apatite coexisting with subhedral–anhedral amphibole and euhedral plagioclase. See Fig. 3 for minerals abbreviations

of 145.5 ± 1.1 Ma (Li et al. 2010b) and 146.1 ± 1.2 Ma (Wen et al. 2020a) for the Lingxiang diorite, respectively.

Chengchao Fe skarn deposit

The Chengchao Fe deposit, containing 280 Mt Fe ores @ 36.1–51.4% wt% Fe, is one of the largest Fe skarn deposits in China (Xie et al. 2012). It is situated in the northern part of the Daye district. The mineralization is mainly associated with diorite and quartz monzonite intruding the evaporite-bearing carbonate of the Middle Triassic Jialingjiang Formation (Fig. 2). Both the diorite and quartz monzonite have been suggested to be genetically associated with the Fe mineralization (Li et al. 2019). The diorite is medium grained, predominantly composed of plagioclase (35–40 vol%), amphibole (20–25 vol%), and minor biotite (5–10 vol%) (Fig. 4d–f), with apatite, zircon, titanite, and magnetite as accessory minerals. The quartz monzonite is medium grained rock which contains plagioclase (40–50 vol%), quartz (30–35 vol%), and minor amphibole (~ 5 vol%). The accessory minerals include apatite, zircon, magnetite, and titanite (Fig. 4g–i).

Both exoskarn and endoskarn are abundant in the Chengchao Fe skarn. The exoskarn consists of diopside with minor garnet, which is overprinted by retrograde phlogopite, tremolite, serpentine, and chlorite. Magnetite is closely associated with retrograde assemblage in the exoskarn and becomes massive toward the marble. The endoskarn occurs as mostly irregular veins that are extensive in the diorite and quartz monzonite. The veins are generally a few centimeters in wide, chiefly consisting of diopside with lesser amounts actinolite, garnet, epidote, and chlorite. U–Pb dating of hydrothermal titanite from skarn ore sample yields an age of 131.2 ± 0.2 Ma (Hu et al. 2017) consistent with $^{40}Ar/^{39}Ar$ age of 133 ± 2 Ma for phlogopite from magnetite ore (Xie et al. 2012). These ages are broadly in agreement with the zircon U–Pb age of 131.6 ± 0.7 Ma and 128.1 ± 1.2 Ma for the diorite and quartz monzonite, respectively (Wen et al. 2020a).

Samples and analytical procedures

Samples

Samples of the ore-related intrusive rocks were collected from surface outcrops and drill cores with sampling locations shown in Fig. 1. The Jinniu basin basalts represent the most primitive igneous rocks in Daye district, which were also collected for the purpose of apatite trace element modeling (see below). The fresh granitoids samples were selected for apatite separation and whole-rock analyses as well as thin section production. Two types of thin sections were made. The normal thin sections (30–40 µm) were used for petrographic observation and the thick sections (100–120 µm) were used for laser ablation analysis. Apatite grains were separated from fresh granitoid whole-rock samples using standard heavy-liquid and magnetic methods and then these grains were examined under a binocular microscope to select clear grains. Next, the selected apatite grains were mounted in epoxy and polished to the core center. Prior to in situ analyses, apatite was identified using optical microscopy, and then imaged by backscattered electron (BSE) and cathodoluminescence (CL) (Fig. 5). Apatite grains hosted in the thick sections and epoxy are used for in situ compositional and isotopic analyses.

Electron microprobe (EMP) analysis

Quantitative EMP analyses were conducted using a JEOL JXA-8230 superprobe equipped with wavelength-dispersive spectrometers at the Center for Material Research and Analysis, Wuhan University of Technology, China. The operating condition was set at 15 kV accelerating voltage, probe current of 20 nA, and a beam diameter of 5 µm. The analysis points preferentially selected apatite grains oriented with the *c*-axis parallel to the incident electron beam, to minimize the effects of EMP-operating conditions on the halogen intensities (Stock et al. 2015). The F, Cl and Ca were measured first with counting times of 10 s for peak after 5 s for background to minimize the effects of EMP-operating conditions on halogen intensities. The remaining elements were analyzed subsequently with longer counting times on the peak positions (40 s for La, Ce and S; 20 s for P, As, V, Si, Ti, Al, Ca, Mg, Mn, Fe, and K; and 10 s for Na). The standard materials used were $Ca_5(PO_4)_3F$ (Ca, P), CaF (F), $Fe_3Al_2Si_3O_{12}$ (Al, Si), $NaAlSi_3O_8$ (Na), $KAlSi_3O_8$ (K), Fe_2O_3 (Fe), $MnSiO_3$ (Mn), $BaSO_4$ (S), $SrSO_4$ (Sr), $Na_4AlBeSi_4O_{12}Cl$ (Cl), $(Mg, Fe)_2SiO_4$ (Mg), $(Ce, La, Y, Th)PO_4$ (La, Ce). Durango and Madagascar apatite were analyzed as a secondary standard, and the data agree well with the recommended values and the precision was better than 5% for most of the elements. The major element concentrations of Durango and Madagascar apatite are listed in Supplementary Table 1. Method from Ketcham (2015) was used to calculate the apatite chemical formula.

LA-ICP-MS trace element analysis

The trace elements in apatite were measured with a laser ablation-inductively coupled-plasma mass spectrometry (LA-ICP-MS) at the Wuhan SampleSolution Analytical Technology Co., Ltd., Wuhan, China. The detailed analytical procedure was described by Zong et al. (2017). An Agilent 7700e ICP-MS instrument with helium as the carrier gas was used to acquire ion-signal intensities. The laser ablation spots and frequency were set to 44 µm and 10 Hz. Each group of 8 apatite analyses was bracketed by analyses of glass NIST 610 to correct signal drift. The international basalt glass standards NIST BCR-2G, BHVO-2G and BIR-1G were used as external standards. Element concentrations were calibrated against multiple-reference materials without applying internal standardization (Liu et al. 2008). To determine experimental accuracy and precision, Madagascar and Durango apatite were analyzed as a secondary standard. These apatite data agree well with the recommended values. Data reduction was performed using the in-house software ICPMSDataCal (Liu et al. 2008). The trace element concentrations of NIST SRM 610, Durango and Madagascar apatite during this study are listed in Supplementary Table 2.

LA-MC-ICP-MS Sr–Nd isotopic analysis

In situ Sr–Nd isotope analysis of apatite was measured by a Neptune Plus MC-ICP-MS connected with Geolas HD excimer ArF laser ablation system at the State Key Laboratory of Geological Processes and Mineral Resources, China University of Geosciences, Wuhan. Helium was used as the carrier gas to transport the ablated materials and then mixed with purified argon and nitrogen before entering the ICP torch. For in situ apatite Sr isotope, the spot diameter of the laser was 90 and 120 µm, which is dependent on Sr signal intensity and apatite granular size. The pulse frequency was 10 Hz and the laser fluence was kept constant at ~ 10 J/cm^2. For in situ apatite Nd isotope measurements, the spot diameter of the laser was 60 and 90 µm depending on Nd signal intensity and apatite granular size. The pulse frequency was 8 Hz and the laser fluence was ~ 8 J/cm^2. Two natural apatites, Durango and Madagascar were used as the second standard to verify accuracy of the calibration method for in situ Sr and Nd isotope analysis of apatite. The Sr and Nd isotopic compositions of Durango and Madagascar have been reported by Yang et al. (2014). All data reduction for the MC-ICP-MS analysis of Sr and Nd isotope

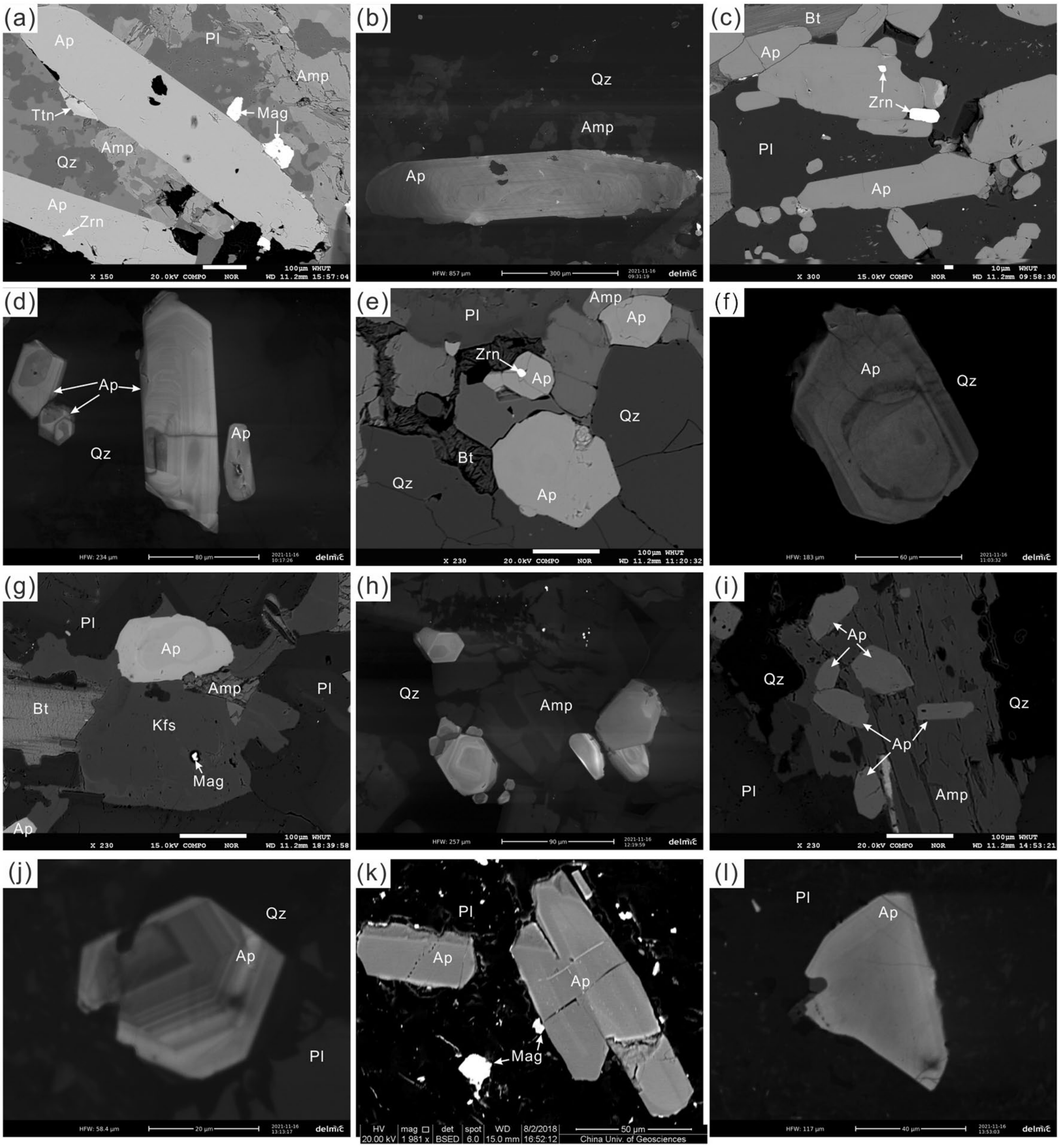

Fig. 5 Representative BSE and CL images of apatite grains from the Cu- and Fe-related granitoids and Jinniu basalt. **a** BSE image of prismatic apatite in Tongshankou granodiorite, coexisting with the amphibole and quartz. **b** Prismatic apatite from Tongshankou granodiorite showing oscillatory zoning textures under CL. **c** Euhedral apatite crystals from Ruanjiawan quartz diorite are homogeneous under BSE and some have zircon inclusions. **d** CL image of apatite crystals from Ruanjiawan quartz diorite showing zoning texture. **e** Euhedral apatite crystals from Tonglushan quartz diorite are homogeneous under BSE. **f** CL image showing zoning texture of apatite crystal from Tonglushan quartz diorite. **g** Euhedral apatite coexisting with plagioclase and amphibole in Lingxiang diorite. **h** Apatite crystal from Lingxiang diorite showing zoning texture under CL. **i** Euhedral apatite hosted in amphibole in Chengchao diorite. **j** CL image showing zoning texture of columnar apatite in Chengchao quartz monzonite. **k** BSE images showing zoning texture of apatite crystals from Jinniu basalt. **l** CL image showing zoning texture of apatite in Jinniu basalt. See Fig. 3 for minerals abbreviations

ratios was conducted using "Iso-Compass" software (Zhang et al. 2020a). In situ apatite Sr–Nd isotopic composition are listed in Supplementary Table 3. The Durango apatite in this study yielded a weighted mean of $^{87}Sr/^{86}Sr = 0.706317$ and $^{143}Nd/^{144}Nd = 0.512477$, respectively. The Madagascar apatite in this study yielded a weighted mean of $^{87}Sr/^{86}Sr = 0.711805$ and $^{143}Nd/^{144}Nd = 0.511348$, respectively. The Sr–Nd isotopic compositions of standards of Durango and Madagascar apatite in this study are listed in Supplementary Table 3. The analytical uncertainties were $< 0.015\%$ for $^{87}Sr/^{86}Sr$ and $< 0.005\%$ for $^{143}Nd/^{144}Nd$, respectively.

Whole rock S isotopes

The fresh intrusive rocks were selected for whole-rock S isotopes analyses. The whole-rock sulfur isotopes were measured by vacuum-line conversion to SO_2, followed by elemental analyzer (EA)-IRMS in the Analytical Laboratory of Beijing Research Institute of Uranium Geology. Details of the analytical procedures have been described in Liu et al. (2013). The results are reported in standard δ notation in ‰ relative to Canyon Diablo troilite (CDT). The reproducibility of $\delta^{34}S$ values was ± 0.2 ‰.

Results

Apatite petrography

Representative microscopic, BSE and CL images of apatite from the Cu- and Fe-related intrusions and Jinniu basin basalts are presented in Figs. 3, 4 and 5. Apatite grains from Cu skarn-related intrusions are euhedral to subhedral and mostly 50–500 μm in size, which commonly occur as inclusions hosted in other major phase such as amphibole, plagioclase, and biotite (Fig. 3). The majority of the apatite crystals show homogenous texture in the BSE images and oscillatory zoning textures in CL images (Fig. 5a–f). Some of the apatite grains have fractures developing along the grain edges or close to mineral inclusions (e.g., zircon) within the gain (Fig. 5a, c, e). Apatite from the Tongshankou granodiorite is columnar and prismatic, with aspect ratios ranging from 6:1 to 2:1 and size up to 500 μm (Figs. 3b, c, 5a, b). Apatite crystals from the Ruanjiawan quartz diorite have aspect ratios of 5:1–1:1. They are mostly in columnar shape and 200–300 μm in size (Figs. 3e, f, 5c, d). Apatite grains from the Tonglushan quartz diorite show aspect ratios ranging from 3:1 to 1:1, which are mostly columnar crystals with size of 100–300 μm (Figs. 3h, i, 5e, f).

Apatite grains from Fe skarn-related intrusions are mostly columnar crystals 50–200 μm in size. They mostly occur as inclusions hosted in the plagioclase, amphibole, and biotite (Fig. 4). Majorities of apatite crystals show oscillatory zonation in the BSE and CL images and some of the crystals are homogenous in BSE images (Fig. 5g–j). Mineral inclusions are absent in the apatite grains. Apatite from the Lingxiang diorite is prismatic and 100–200 μm in size with aspect ratios ranging from 6:1 to 1:1 (Figs. 4b, c, 5g, h). Apatite from the Chengchao diorite and quartz monzonite is columnar and 50–200 μm in size with aspect ratios in the range of 4:1–1:1 (Figs. 4e, f, 5i; Figs. 4h, i, 5j).

Apatite grains from Jinniu basin basalts are euhedral to subhedral and mostly columnar crystals 50–100 μm in size with aspect ratios of 10:1–2:1 (Fig. 5k, l). They are mostly present in the groundmass of the basalt with minor crystals hosted in plagioclase (Fig. 5k, l). The majority of apatite crystals were observed to be zoned in BSE and CL images (Fig. 5k, l).

Major and trace element compositions

Results of major and trace element analysis of apatite from the ore-related intrusions and basalts in Jinniu basin are listed in Supplementary Tables 1 and 2, respectively. All the apatite grains from ore-related intrusions have relatively high SiO_2 and low MnO concentrations, which are plotting in the magmatic apatite field in the SiO_2 vs. MnO diagram (Chen and Zhang 2018; Fig. 6). The apatite grains from Cu skarn-related intrusions have higher P + Ca contents than those from the Fe skarn-related intrusions (Fig. 7a). The P and Ca display a negative correlation with the Si, Na, La, and Ce (Fig. 7a), which probably indicates the substitutions $REE^{3+} + Si^{4+} = Ca^{2+} + P^{5+}$ in apatite (Sha and Chappell 1999; Mao et al. 2016). The La, Ce, and S show a positive correlation with the Na and Si (Fig. 7b), which may reflect the substitutions: $REE^{3+} + SiO_4^{4-} = Ca^{2+} + PO_4^{3-}$, $SO_4^{2-} + SiO_4^{4-} = 2PO_4^{3-}$ and $SO_4^{2-} + Na^{+} = PO_4^{3-} + Ca^{2+}$ (Rouse and Dunn 1982; Parat and Holtz 2004). Apatite from Cu-related Tongshankou granodiorite contains F, Cl and SO_3 contents of 2.58–3.23 wt%, 0.11–0.28 wt%, and 0.11–0.22 wt%, respectively. The concentrations of F, Cl, and SO_3 in apatite from Cu-related Ruanjiawan quartz diorite range from 2.45 to 3.00 wt%, 0.04 to 0.13 wt%, and 0.12 to 0.17 wt%, respectively. Apatite from quartz diorite associated with Tonglushan Cu skarn contains F, Cl, and SO_3 concentrations of 2.35–3.19 wt%, 0.17–0.60 wt%,

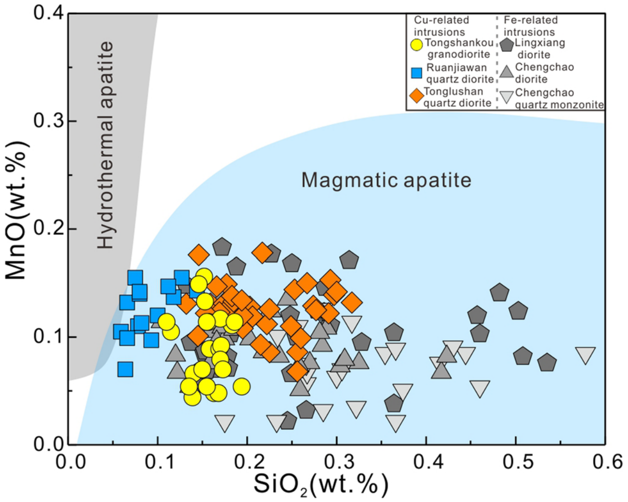

Fig. 6 Apatite SiO_2–MnO plot. The fields of magmatic and hydrothermal apatite are from Chen and Zhang (2018)

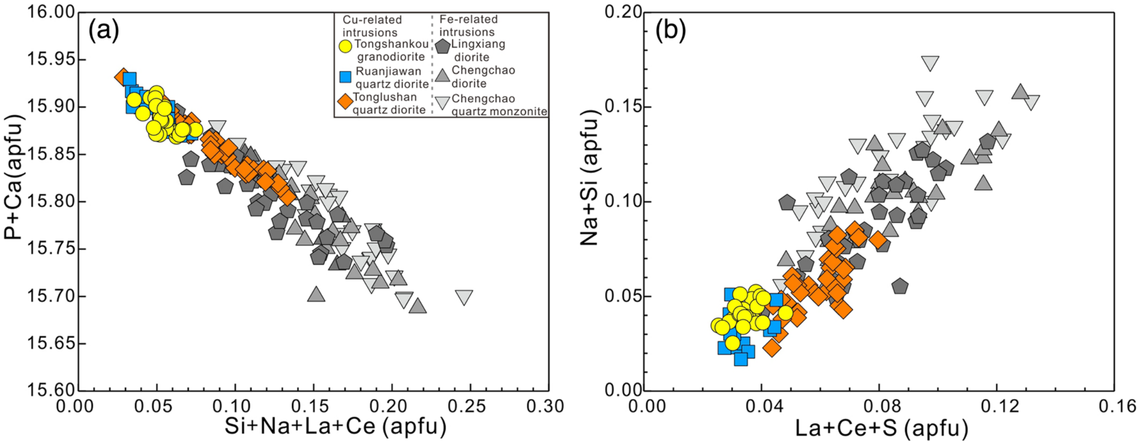

Fig. 7 Apatite compositions calculated to chemical formula (method proposed by Ketcham 2015). **a** (Si + Na + La + Ce) vs. (P + Ca); **b** (La + Ce + S) vs. (Na + Si)

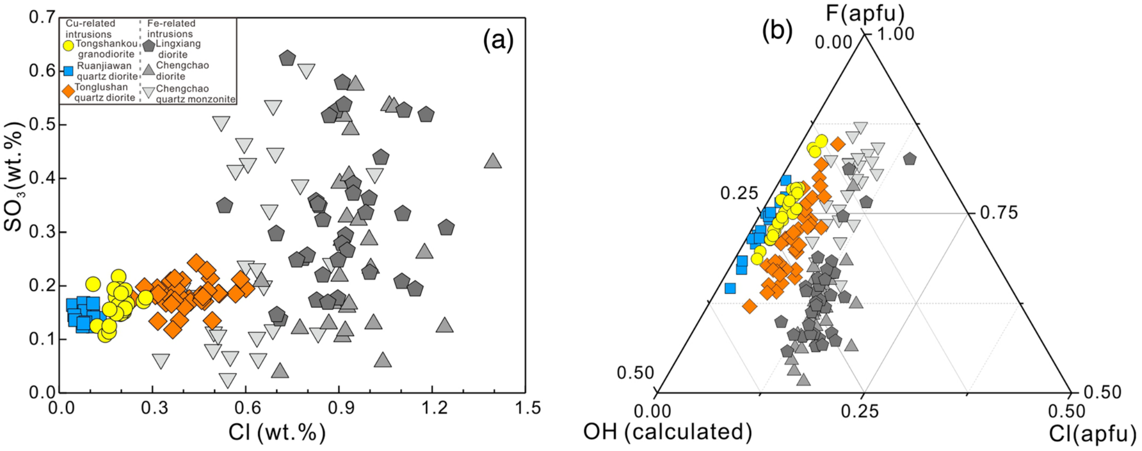

Fig. 8 Binary plots showing the volatile compositional variation of apatite. **a** Apatite SO_3 versus Cl diagram; **b** Apatite F–Cl–OH plot. Apatite F–Cl–OH chemical formula calculated using the method in Ketcham (2015)

and 0.12–0.24 wt%, respectively (Supplementary Table 1). The apatite F, Cl, and SO_3 concentrations are more variable for the Fe-related relative to the Cu-related intrusions (Fig. 8). Apatite from diorite associated with Liangxiang Fe skarn contains F, Cl, and SO_3 concentrations in the range of 2.09–3.07 wt%, 0.53–1.24 wt%, and 0.14–0.62 wt%, respectively. Apatite from intrusions (diorite and quartz monzonite) associated with Chengchao Fe skarn contain F concentrations of 1.93–3.22 wt%, Cl concentrations of 0.33–1.39 wt%, and SO_3 contents of 0.03–0.60 wt% (Supplementary Table 1). In general, apatite from Fe skarn-related intrusions has Cl and SO_3 concentrations that are higher than those of apatite from the granitoids associates with Cu skarn (Fig. 8a). All the apatite crystals are compositionally dominated by fluorapatite. There is no significant difference in apatite F and calculated OH contents between granitoids related to Fe skarns and Cu skarns (Fig. 8).

Apatite from Cu skarn-related granitoids has a wide range in total REE concentrations (ΣREE) but shows similar chondrite-normalized REE patterns with weak to moderate Eu negative anomalies (Fig. 9a–c). The ΣREE of apatite from Cu-related Tongshankou granodiorite, Ruanjiawan quartz diorite, and Tonglushan quartz diorite varies from 2856 to 3670 ppm, 3148 to 5121 ppm and 4788 to 9129 ppm, respectively. In comparison, apatite from Fe skarn-related Lingxiang diorite, Chengchao diorite and quartz monzonite has higher ΣREE concentrations of 4973–14,516 ppm, 5111 to 12,855 ppm, 7331 to 15,351 ppm, respectively. All the apatite grains are depleted in large-ion lithophile element (Rb, Ba,) and high-field-strength element (Nb, Ta, Zr, Hf) relative to whole-rock samples (Fig. 10). The apatite grains from the Cu skarn-related intrusions have Sr concentrations of 446–1139 ppm (764 ppm on average) and Y contents of 161–416 ppm (261 ppm on average), with Sr/Y ratio of

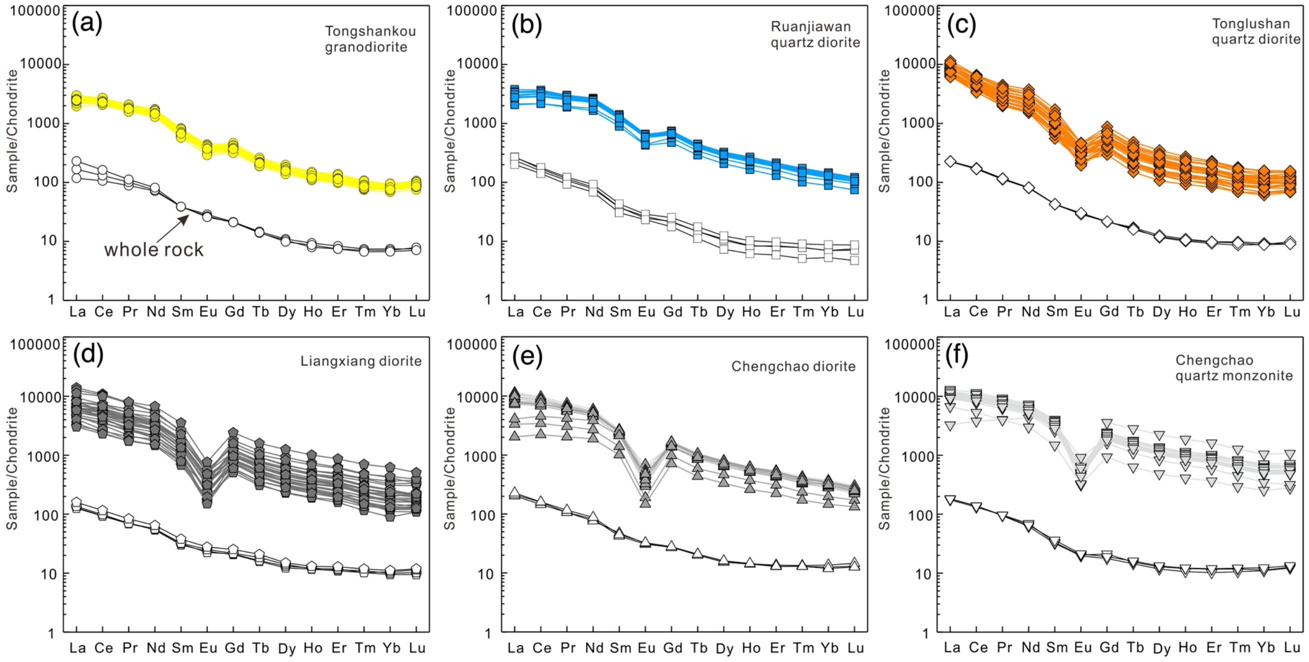

Fig. 9 Chondrite-normalized REE patterns of the apatite and whole-rock samples from the ore-related granitoids in the Daye region. Normalizing values are from McDonough and Sun (1995). Data sources for the whole rocks are from Yan et al. (2012) and Wen et al. (2020a)

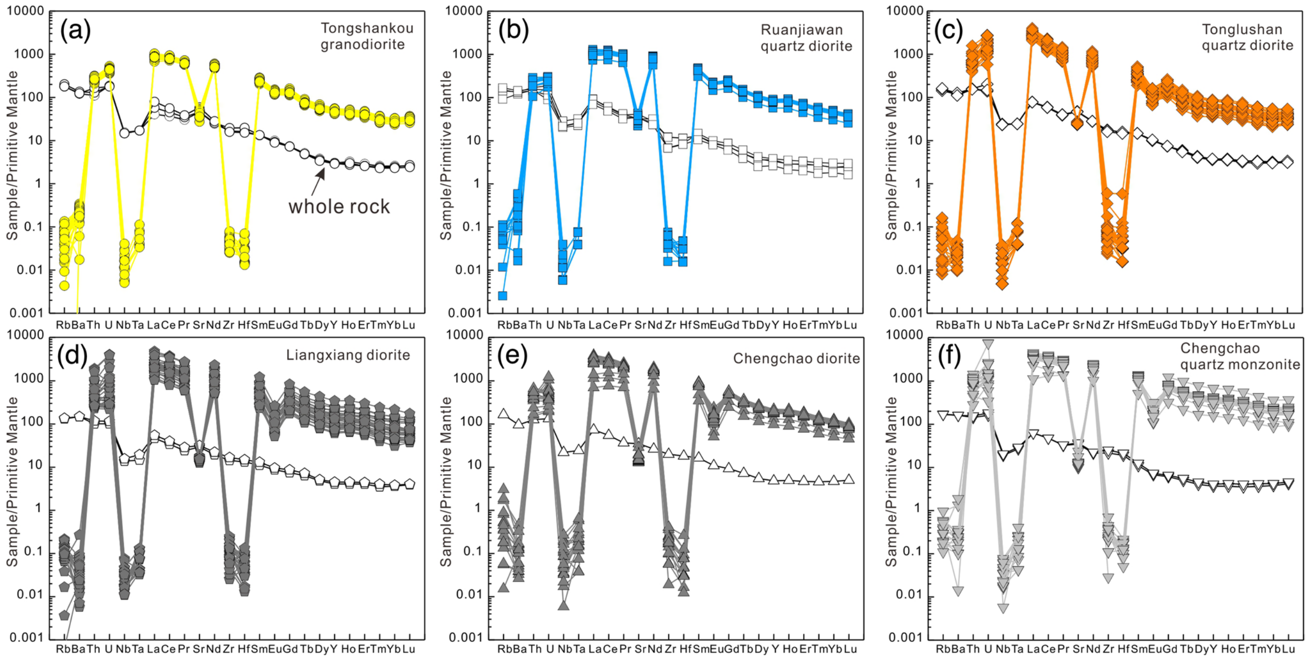

Fig. 10 Primitive mantle-normalized trace elements spider diagrams of the apatite and whole-rock samples from the ore-related granitoids in the Daye region. Normalizing values are from McDonough and Sun (1995). Data sources for the whole rocks are from Yan et al. (2012) and Wen et al. (2020a)

1.16 to 5.71 (Fig. 11). In comparison, the apatite grains from the Fe skarn-related intrusions have lower Sr contents (216–428 ppm, 308 ppm on average) and higher Y (278 to 1944 ppm, 945 ppm on average) and much lower Sr/Y ratio (0.11–1.12) (Fig. 11). The apatite grains from Cu skarn-related intrusions display relatively high Eu/Eu* ratio (Eu/

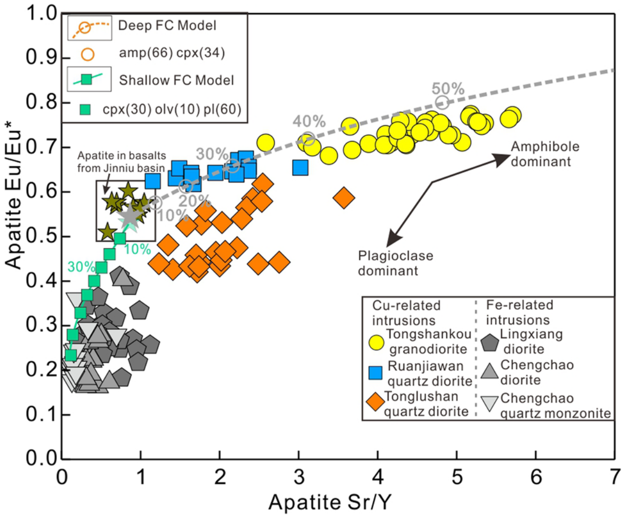

Fig. 11 Apatite Sr/Y and Eu/Eu* ratios and trace element fractional crystallization (FC) models. Labeled values indicate the percentage of crystallization of the mineral assemblage in each model. The start of each fractionation path and percentage of crystallization are from Nathwani et al. (2020). The square with black border shows the location of the apatite from basalts in the Jinniu basin. To reduce the complexity of Eu/Eu* in the modeling, we assume the magmatic oxidation state is at FMQ + 2, where FMQ is the fayalite—magnetite—quartz buffer

Eu* = Eu_N/(sqrt(Sm_N*Gd_N), where "N" refers to chondrite-normalized value). Apatite Eu/Eu* ratios from Cu-related Tongshankou granodiorite, Ruanjiawan quartz diorite, and Tonglushan quartz diorite range from 0.68 to 0.77 (0.73 on average), 0.61 to 0.67 (0.64 on average), 0.40 to 0.61 (0.48 on average), respectively (Fig. 11). The apatite grains from Fe skarn-related Lingxiang diorite, Chengchao diorite, and quartz monzonite have much lower Eu/Eu* ratios, ranging from 0.21 to 0.38 (0.28 on average), from 0.16 to 0.27 (average of 0.21), and from 0.17 to 0.36 (0.22 on average), respectively (Fig. 11).

Apatite from Jinniu basin basalts has CaO and P_2O_5 concentrations ranging from 52.91 to 55.78 wt% and from 39.04 to 41.87 wt%, respectively. It contains F, Cl, and SO_3 concentrations of 2.59–3.52 wt%, 0.04–0.39 wt%, and 0.01–0.29 wt%, respectively (Supplementary Table 1). The concentrations of ΣREE, Sr, and Y in the apatite are in the range of 8495–17,623 ppm, 779–987 ppm, and 819–1696 ppm, respectively. It has Sr/Y and Eu/Eu* ratios of 0.58–1.05 and 0.51–0.60, respectively (Supplementary Table 2; Fig. 11).

Sr and Nd isotopic compositions

Strontium and Nd isotopic compositions of the apatite are listed in Supplementary Table 3. The initial Sr isotopic ratios (I_{Sr}) and $\varepsilon_{Nd}(t)$ values of apatite grains are calculated using the zircon U–Pb age of the apatite-hosting intrusions from previous studies (Wen et al. 2020a; Deng et al. 2015). The apatite grains from the Cu-related intrusions have relatively homogenous Sr–Nd isotopic compositions. The apatite grains from Cu-related granitoids at Tongshankou,

Fig. 12 $^{87}Sr/^{86}Sr$ ratio of apatite and whole-rock samples. Data sources for the whole rocks are from Li et al. (2009, and references therein), and Xie et al. (2015, and references therein). Middle Triassic seawater $^{87}Sr/^{86}Sr$ ratios are from Song et al. (2015)

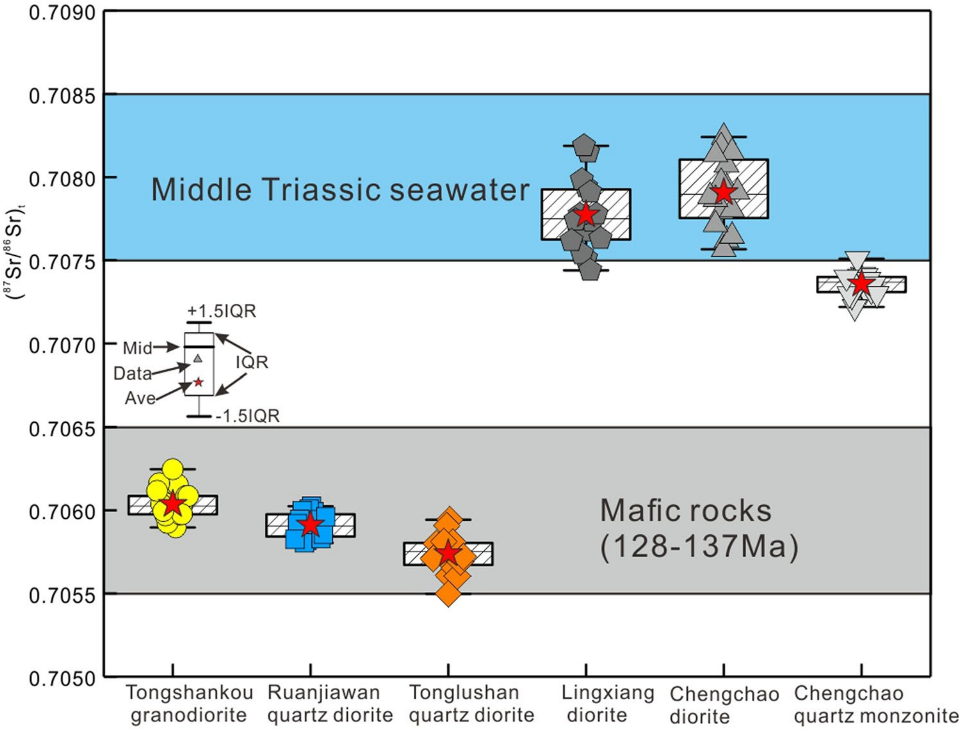

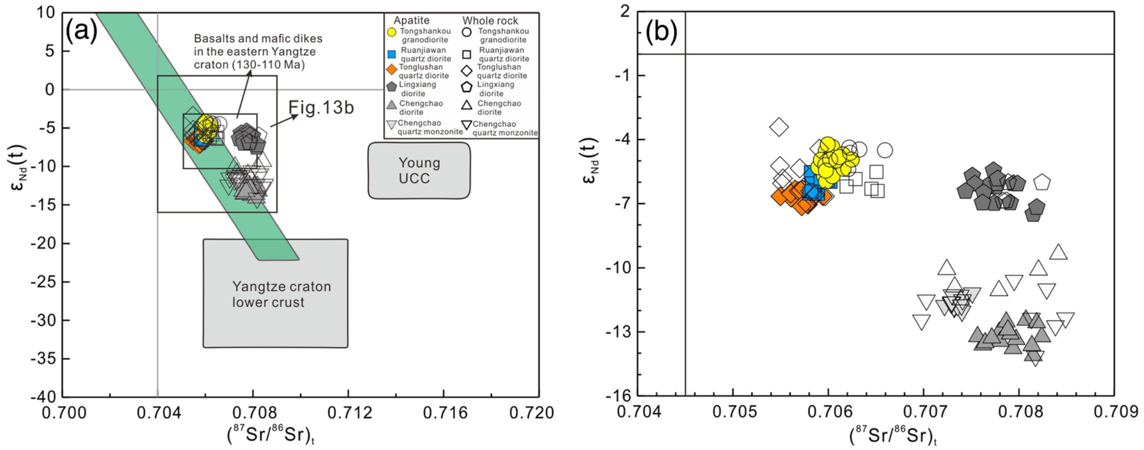

Fig. 13 Apatite and whole-rock initial $^{87}Sr/^{86}Sr$ versus $\varepsilon_{Nd}(t)$ plot. Data sources for the whole rocks are from Li et al. (2009, and references therein), and Xie et al. (2015, and references therein)

Ruanjiawan and Tonglushan have calculated $(^{87}Sr/^{86}Sr)_t$ values of 0.7059–0.7061 (0.7060 on average), 0.7058–0.7060 (0.7059 on average), 0.7055–0.7059 (0.7057 on average), respectively (Fig. 12). The calculated $\varepsilon_{Nd}(t)$ values for apatite from Tongshankou, Ruanjiawan and Tonglushan range from − 5.97 to − 5.35 (− 5.13 on average), from − 6.54 to − 5.52 (− 6.02 on average) and from − 7.12 to − 5.98 (− 6.57 on average), respectively (Fig. 13). The apatite grains from Fe-related Lingxiang diorite, Chengchao diorite, and Chengchao quartz monzonite have comparable $(^{87}Sr/^{86}Sr)_t$ values, which range from 0.7074 to 0.7082 (0.7078 on average), from 0.7076 to 0.7082 (0.7079 on average), and from 0.7072 to 0.7075 (0.7074 on average), respectively (Fig. 12). The apatite $\varepsilon_{Nd}(t)$ values are − 7.50 to − 5.45 (− 6.39 on average), − 14.11 to − 12.45 (− 13.23 on average), and − 12.04 to − 11.18 (− 11.57 on average) for Lingxiang diorite, Chengchao diorite and Chengchao quartz monzonite, respectively (Fig. 13).

Whole rock sulfur isotope data

The result of whole-rock sulfur isotopic analyses from this study together with previous published sulfur isotopes of sulfide are summarized in Supplementary Table 4 and shown in Fig. 14. The Cu-related Tongshankou granodiorite, Ruanjiawan quartz diorite and Tonglushan quartz diorite have $\delta^{34}S_{V\text{-}CDT}$ values of + 3.4 to 4.7‰, + 2.8 to + 5.8‰, and + 5.2 to + 7.4‰, respectively. The Fe skarn-related igneous rocks have much higher $\delta^{34}S_{V\text{-}CDT}$ values than the Cu-related equivalents. The diorite and quartz monzonite associated with Chengchao Fe skarn have $\delta^{34}S_{V\text{-}CDT}$ values ranging from + 8.3 to + 11.9‰ and from + 10.9 to + 13.7‰, respectively. The diorite related with Lingxiang Fe skarn displays $\delta^{34}S_{V\text{-}CDT}$ values of + 15.2 to + 16.3‰.

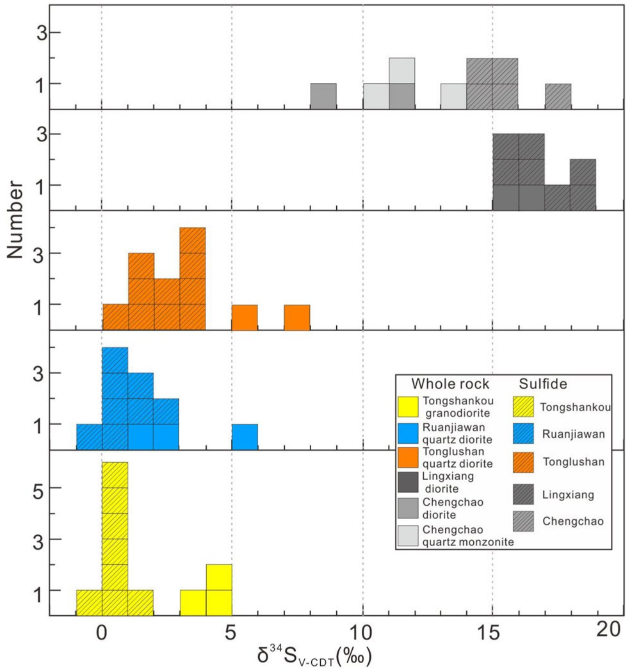

Fig. 14 Histogram of sulfur isotopic compositions for whole rocks and sulfides from the skarn deposits of the Daye district. Data sources for sulfides are listed in the Supplementary Table 4

Discussion

Magma source revealed from apatite Sr–Nd isotopes

Apatite Sr and Nd isotope compositions have been increasingly utilized as a useful tool to trace magma source (Sun et al. 2019, 2021; Zhang et al. 2020b; Cao et al. 2021). Apatite from the ore-related intrusions under investigation has

$(^{87}Sr/^{86}Sr)_t$ and $\varepsilon_{Nd}(t)$ values ranging from 0.7055 to 0.7085 and from − 15 to − 5, respectively, which are well consistent with previous published Sr–Nd isotope data of whole-rock samples of the apatite-hosting intrusions (Fig. 13a). The Sr–Nd isotopes of apatite from the ore-related intrusions is significantly different from that of the lower crust of the Yangtze craton (Fig. 13a), precluding the possibility that the ore-related intrusions were directly derived from the ancient lower crust. The granitoids associated with Cu skarn and Lingxiang Fe skarn have apatite and whole-rock $\varepsilon_{Nd}(t)$ values similar to that of the contemporaneous basaltic andesite and mafic dike in Daye and adjacent areas in the MLYMB (Fig. 13a), which were derived from an enriched lithospheric mantle (Xie et al. 2008; Li et al. 2009, 2013a). The diorite and quartz monzonite associated with Chengchao Fe skarn, have lower apatite and whole-rock $\varepsilon_{Nd}(t)$ values of − 14 to − 11 and − 15 to − 9 (Fig. 13b), respectively, probably reflecting greater contributions from the ancient lower crustal materials. Both apatite and whole-rock samples of Fe skarn-related granitoids have $(^{87}Sr/^{86}Sr)_t$ values that are systematically higher than those of Cu skarn-related counterparts (Fig. 13), suggesting additional input of upper crust components that enriched in radiogenic Sr for the Fe skarn-related granitoids. The evaporite-bearing Middle Triassic carbonate of Jialingjiang Formation is the main host of the Fe skarn deposits in Daye district, which contains high Sr contents (2332 ppm on average; Li et al. 2014b) with relatively high $(^{87}Sr/^{86}Sr)_t$ ratios (Fig. 12). The relative enriched Sr isotopic composition for the Fe skarn-related granitoids may be attributed to larger extents of wall rock assimilation during the time of magma emplacement into the evaporite-bearing Middle Triassic Jialingjiang Formation.

Apatite Sr/Y and Eu/Eu* ratios record magma evolution path

Apatite in magmatic systems responds compositionally to changing melt composition and preserve a wealth of information on magma evolution history (Sha and Chappell 1999; Bruand et al. 2014, 2016; Nathwani et al. 2020). Fractional crystallization is one of the dominant magmatic processes shifting melt compositions, which can be readily recorded by apatite (Bruand et al. 2016; Nathwani et al. 2020; Zhang et al. 2020b). It is noteworthy that temperature and melt composition affect apatite-melt partition coefficients, but they exert much less influence on partition coefficient ratios (Prowatke and Klemme 2006). Thus, apatite element ratios are considered as a more robust tool in tracing magma evolution process (Nathwani et al. 2020).

Hydrous magma with high Sr/Y and Eu/Eu* ratios likely has experienced fractionation of amphibole and/or garnet, but suppressed of plagioclase crystallization in the deep crust (Defant and Drummond 1990; Richards and Kerrich 2007). Apatite grains crystalizing from such magma generally inherit the elevated Sr/Y and Eu/Eu* ratios (Nathwani et al. 2020). The apatite from the Cu skarn has significantly higher Sr/Y and Eu/Eu* ratios than that of the apatite from the Fe skarn (Fig. 11), which is consistent with previous published whole-rock data that the Sr/Y and Eu/Eu* ratios for intrusions associated with Cu skarn are generally higher than the Fe skarn-related counterparts (Xie et al. 2008; Li et al. 2009; Wen et al. 2020a). The elevated whole-rock Sr/Y (> 60) and Eu/Eu* (> 0.8) have been attributed to high ratios of amphibole/plagioclase fractionation for the Cu skarn-related intrusions (Li et al. 2009; Wen et al. 2020a).

To further investigate the magma evolution through apatite Sr/Y and Eu/Eu* ratios, we apply the trace element fractionation modeling from Nathwani et al. (2020), which includes deep (high pressure) and shallow (low pressure) evolution models distinguished by different fractionation assemblages used for the modeling. The fractionation assemblage consisting of 66% amphibole and 34% clinopyroxene is set for the deep evolution model; for the shallow evolution model, the fractionation/crystallization assemblage composed of 30% clinopyroxene, 10% olivine, and 60% plagioclase is used (Nathwani et al. 2020). It has been suggested that the ore-related intrusive rocks in Daye district are sourced from basaltic melts that were derived from an enriched lithospheric mantle (Li et al. 2009). Therefore, we use the compositions of apatite from the basalts in Jinniu basin to approximate the composition of apatite crystalized from the parental melt of the ore-related intrusive rocks, which represent the starting points in the modeling (Fig. 11). Though this is a simplified approach, the modeling may qualitatively illustrate the magma evolution paths for ore-related intrusions. The apatite from the Cu-related granitoids displays a compositional trend consistent with that predicted from the deep evolution model, in which amphibole is a dominant fractionation phase (Fig. 11). The amphibole fractionation process is also evidenced by the elevated zircon Yb/Dy (3.5–8.6, 6.2 on average) and Eu/Eu* (0.29–0.87, 0.64 on average) ratios for the Cu-related granitoids (Wen et al. 2020a). In contrast, the apatite from the Fe skarn-related granitoids has composition following that predicted from the shallow evolution model, in which plagioclase dominates the fractionation/crystallization assemblage, consistent with relatively low zircon Yb/Dy (2.6–5.6, 3.8 on average) and Eu/Eu* (0.27–0.44, 0.36 on average) ratios for the intrusions associated with the Fe skarn (Wen et al. 2020a). The apatite trace element modeling is consistent with previous whole rock and zircon geochemistry studies indicating that the magmas associated with the Cu mineralization may have experienced amphibole-dominated fractionation in the deep crust, whereas those responsible for the Fe skarns have undergone plagioclase-dominated fractionation/crystallization in shallower level.

Magma volatile compositions

Volatile compositions (S, Cl, and F) play an important role for metal productive magmas, because they can facilitate hydrothermal mobilization and concentration of metals (Holland 1972; Yardley 2005), and halogens (Cl, F in particular) can effectively reduce solidus temperatures (Manning 1981; Keppler 1993), the viscosity and ion diffusivity of melts (Dingwell et al. 1985; Giordano et al. 2004). However, primary volatile (S, Cl, and F) compositions in magmas are not be directly reflected by whole-rock volatiles (S, Cl, and F) contents, as these elements strongly partition into the volatile phases and likely to be lost during magma degassing (Webster et al. 2009; Parat et al. 2011; Wang et al. 2018). Previous studies have successfully used apatite to investigate the volatile budget of magmas based on experimentally constrained apatite-melt partitioning (Webster et al. 2009; Parat et al. 2011; Chelle-Michou and Chiaradia 2017; Cao et al. 2022). To make an estimation on melt halogen composition, we apply the partition coefficients of F and Cl between apatite and felsic melts at ~ 200 MPa and 900–924℃ from experiments of Webster et al. (2009), the P–T condition of which are assumed to approximate that of the ore-related melts at the time of apatite crystallization. We further apply the methods from Peng et al. (1997) and Parat et al. (2011), respectively, to calculate melt S contents for the ore-related granitoids.

The calculated melt volatile compositions are listed in Table 1. The Cu-related intrusions have calculated F concentrations ranging from 1553 to 2136 ppm, which are similar to that of the Fe-related intrusions (1277 to 2134 ppm). The calculated S concentration, based on the method of Peng et al. (1997), ranges from 145 to 354 ppm and from 20 to 529 ppm for the Cu-related and Fe-related intrusions, respectively. While using the method of Parat et al. (2011), the calculated S concentration is lower, ranging from 16 to 36 ppm and 9 to 406 ppm for the Cu-related and Fe-related granitoids, respectively. The reason for this discrepancy is not clear but both the calculations indicate a much wider range of magma S contents for the Fe-related granitoids relative to the Cu-related counterparts (Table 1). The calculated Cl concentration for intrusions associated with the Cu skarn ranges from 430 to 5990 ppm (2711 ppm on average), which is comparable to that of Cu porphyries (230–5420 ppm) in the Tethyan metallogenic belt (Xu et al. 2021) as well as that of basaltic magmas from the arc and back-arc (100–4100 ppm) (Wallace 2005). The Fe skarn-related intrusions have calculated Cl concentration ranging from 3260 to 13,940 ppm, with an average of 8386 ppm, significantly higher than that of the Cu skarn-related equivalents. This observation suggests that magmatic-hydrothermal fluids exsolved from the Fe skarn-related intrusions may have provided sufficient Cl, which facilitates effective transportation of Fe to form magnetite ores. This consideration is based on existing knowledge that Fe is predominantly complexed by chloride at magmatic-hydrothermal conditions (Simon et al. 2004; Bell and Simon 2011; Scholten et al. 2019).

Potential role of wall rock assimilation

Iron skarn deposits in the Daye district are mostly hosted by the Middle Triassic Jialingjiang Fm., which contains abundant evaporitic rocks mainly composed of gypsum and/or anhydrite, halite, and other salts minerals (Cai 1980; Li et al. 2013b; Xie et al. 2020). Previous sulfur isotopic studies have shown that sulfides from the Cu skarn deposits have δ^{34}S values ranging from − 6.2 to + 8.7‰ (averaging + 1.2‰) whereas the values are + 10.3 to + 20.0‰ (averaging + 16.2‰) for Fe skarn deposits (Supplementary Table 4; Fig. 14). This contrasting sulfur isotopic compositions can be best interpreted in terms of significant contribution of sulfur from the evaporite sulfate in the process of Fe skarn mineralization (Xie et al. 2015; Zeng et al. 2020). Such a process, however, was absent or weak in the formation of Cu skarn deposits. Our new whole-rock sulfur isotope data further demonstrate that the Fe-related intrusions may have assimilated greater amount of evaporite-bearing Middle Triassic carbonate (Supplementary Table 4; Fig. 14). This view is further supported by apatite Sr isotope data, with much higher initial Sr isotopic ratios for the granitoids related to Fe skarn than the Cu skarn (Fig. 12). The evaporites are also enriched in Cl, magmatic assimilation of which must have increased Cl contents in the magmas. Such a scenario is consistent with the higher calculated Cl contents for intrusions associated with Fe skarn relative to Cu skarn (Table 1).

The Sr/Y and Eu/Eu* ratios of apatite and modeling results (Fig. 11) reveal that the Cu skarn-related intrusions may have experienced significant amphibole fractionation and suppression of plagioclase crystallization under high pressure and hydrous conditions ($H_2O > 4$ wt%) (Richards 2011; Wen et al. 2020a), whereas those Fe skarn-related counterparts are dominated by plagioclase fractionation at relative low pressure and dry conditions. This inference is consistent with zircon geochemistry that the intrusions associated with Fe skarn have relatively low zircon Yb/Dy (< 0.56) and Eu/Eu* (< 0.44) ratios indicative of relatively dry magmas (Lu et al. 2016; Wen et al. 2020a). In skarn systems, assimilation of carbonate rocks by magmas and related decarbonation reactions could have enhanced the CO_2 contents in the silicate melts (Meinert et al. 2005), which promoted H_2O to be partitioned into the exsolved fluids (Holloway 1976; Meinert et al. 2005). Assimilating

Table 1 Composition of volatile elements in apatite grains and the calculated melt Cl, F and S concentrations

Sample	Apatite Cl (wt%) (average) [median]	Apatite F (wt%) (average) [median]	Apatite S (ppm) (average) [median]	Cl in melts (ppm) (average) [median][a]	F in melts (ppm) (average) [median][a]	S in melts (ppm) (average) [median][b]	S in melts (ppm) (average) [median][c]
Tongshankou granodiorite ($n = 26$)	0.108–0.277 (0.191) [0.194]	2.580–3.226 (2.863) [2.833]	430–870 (650) [640]	1080–2770 (1905) [1940]	1709–2136 (1896) [1876]	176–354 (267) [263]	15–30 (22) [21]
Ruanjiawan quartz diorite ($n = 16$)	0.043–0.130 (0.086) [0.085]	2.447–2.998 (2.742) [2.733]	500–670 (570) [560]	430–1300 (864) [845]	1621–1985 (1816) [1810]	200–271 (232) [227]	17–22 (19) [19]
Tonglushan quartz diorite ($n = 38$)	0.171–0.599 (0.404) [0.397]	2.345–3.191 (2.695) [2.689]	470–970 (730) [720]	1710–5990 (4042) [3970]	1553–2113 (1785) [1781]	145–298 (223) [222]	16–36 (25) [24]
Lingxiang diorite ($n = 38$)	0.531–1.244 (0.903) [0.896]	2.093–3.065 (2.375) [2.359]	550–2500 (1320) [1260]	5310–12,440 (9027) [8955]	1386–2030 (1573) [1562]	87–393 (208) [199]	18–406 (91) [57]
Chengchao diorite ($n = 28$)	0.649–1.394 (0.956) [0.928]	1.928–2.956 (2.285) [2.295]	150–2300 (1070) [900]	6490–13,940 (9564) [9280]	1277–1958 (1513) [1520]	20–300 (140) [118]	10–295 (71) [32]
Chengchao quartz monzonite ($n = 26$)	0.326–1.394 (0.623) [0.621]	2.411–3.223 (2.903) [2.989]	110–2420 (1030) [870]	3260–10,140 (6232) [6205]	1596–2134 (1923) [1979]	24–529 (225) [189]	9–357 (72) [30]

[a] Melt Cl and F concentrations are calculated based on $D_F^{\text{apatite/melt}} = 15.1$ and $D_{Cl}^{\text{apatite/melt}} = 1$ from Webster et al. (2009), where $D_F^{\text{apatite/melt}}$ and $D_{Cl}^{\text{apatite/melt}}$ are apatite-melt partition coefficients for F and Cl, respectively

[b] Estimated from apatite SO_3 contents using the apatite-melt partition coefficient formula of Peng et al. (1997); Apatite saturation temperature (AST) and apatite-melt partition coefficient are listed in Supplementary Table 5

[c] Estimated from apatite SO_3 contents using the apatite-melt partition coefficient formula of (Parat et al. 2011): SO_3 apatite (wt%) = 0.157 × ln SO_3 melt (wt%) + 0.9834

evaporite-bearing carbonate rock by Fe skarn-related magmas may, therefore, not only have contributed to the generation of large amounts of magmatic fluid but also have provided sufficient Cl and SO_4^{2-} so that Fe^{2+} could be effectively transported and subsequently oxidized to form magnetite ores (Bell and Simon 2011; Scholten et al. 2019; Li et al. 2013b; Wen et al. 2017, 2020b). Assimilation of evaporite-bearing wall rocks has also been identified in magmas associated with Fe oxide-apatite deposits in the Ningwu district of the MLYMB, by an integrated fluid inclusion and sulfur isotope investigation of Li et al. (2015). The whole-rock geochemical and Sr–Nd-Pb isotopic study of intermediate intrusions in the Luxi district, North China Craton also revealed significant assimilation of Ordovician evaporitic carbonate by the ore-related magmas that generated a dozen of Fe skarn deposits (Lan et al. 2019).

Apatite as an indicator for mineral exploration

Apatite has been considered as a useful tool in discriminating between barren and fertile intrusions at an early stage of exploration (e.g., Belousova et al. 2002; Mao et al. 2016). The apatite crystals from the Cu-related intrusions in the Daye district have relatively high Sr/Y (1.2–5.7) and Eu/Eu* (0.40–0.77) ratios, which are comparable to those of apatite from the Cu-fertile porphyries in the Sanjiang metallogenic belt in southwestern China (Sr/Y = 0.38–5.57; Eu/Eu* = 0.41–0.88, Pan et al. 2016), Xiongcun district in the southern Tibet (Sr/Y = 0.23–0.92; Eu/Eu* = 0.36–0.90, Xie et al. 2018) and Baguio district of the Philippines (Sr/Y = 0.35–2.28; Eu/Eu* = 0.62–1.21, Cao et al. 2021). The Fe skarn-related intrusions in the Daye district have relatively low apatite Sr/Y and Eu/Eu* ratios ranging from 0.11 to 1.12 and 0.16 to 0.38, respectively, which are comparable to the Cu-barren granitoids in the Sanjiang metallogenic belt in southwestern China (Sr/Y = 0.05–0.60; Eu/Eu* = 0.10–0.33, Pan et al. 2016). Our results, therefore, suggest that the low apatite Sr/Y and Eu/Eu* signature is not necessarily associated with barren intrusions (though Cu-barren is true, this study), but it can be associated with intrusions related to Fe mineralization. The Fe skarn-related intrusions in the Daye district have apatite Cl and SO_3 concentrations mostly higher than 0.5 and 0.1 wt%, whereas the apatite from barren intrusions in Sanjiang region has Cl and SO_3 concentrations generally lower than 0.1 and 0.05 wt%, respectively (Pan et al. 2016). Considering the importance of Cl in hydrothermal mobilization of Fe (Simon et al. 2004; Bell and Simon 2011; Scholten et al. 2019) and sulfate in oxidizing ferrous Fe to form magnetite (Li et al. 2013b; Wen et al. 2017), magmatic apatite with low Sr/Y and Eu/Eu* but high Cl and SO_3 contents may be indicative for Fe-fertile intrusions.

Conclusions

In situ geochemical and isotopic investigations of apatite from granitoid intrusions associated with Cu and Fe skarn deposits in the Daye district provide new insights into the source, evolution and volatile composition of the ore-related magmas. The apatite Sr–Nd isotopes demonstrate that the granitoids associated with Cu skarn were sourced from an enriched lithospheric mantle source, whereas those associated with Fe skarn were derived from a similar source but experienced significant crustal contaminations. The Fe skarn-related intrusions may have assimilated significant amount of evaporite-bearing carbonate rocks upon emplacement, evidenced by their elevated whole-rock $\delta^{34}S$ and apatite $(^{87}Sr/^{86}Sr)_t$ values. Fractionation modeling based on apatite Sr/Y and Eu/Eu* ratios suggests that magmas for the Cu skarn have experienced amphibole-dominated fractionation in the deep crust, whereas those for Fe skarn are dominated by plagioclase fractionation in the shallower environment. The Fe-related granitoids have calculated Cl higher than those associated with Cu skarn, which probably resulted from assimilating larger amount of evaporites. This assimilation process could have facilitated exsolution of large amounts of Cl and sulfate-rich fluids that scavenge Fe from the cooling magma and further oxidize ferrous Fe to form magnetite ores. This study highlights that apatite is a sensitive petrogenetic-metallogenic indicator in skarn systems and can be useful in exploration.

Supplementary Information The online version contains supplementary material available at https://doi.org/10.1007/s00410-022-01890-0.

Acknowledgements This study was financially supported by the National Natural Science Foundation of China (42172101, 41802114), Hubei Geological Bureau (grants KJ2019-5, KJ2021-9) and the 111 project (grant B20045). We thank Shang-Gang Jin, Dong-Qin Liu, Wei-Wei Yang, Guo-Fei Yu, Yue Sun, Ying-Kun Qi and Liang Fan for their help during the field work, and Xiao-Lei Nie and Mei-Jun Yang for assistance with the apatite EMP analysis. Three anonymous reviewers are thanked for their valuable comments and suggestions that improved this paper significantly. Hans Keppler is thanked for editorial handling. This is contribution 65 from CUG Center for Research in Economic Geology and Exploration Targeting (CREGET).

References

Bell AS, Simon A (2011) Experimental evidence for the alteration of the $Fe^{3+}/\Sigma Fe$ of silicate melt caused by the degassing of chlorine-bearing aqueous volatiles. Geology 39(5):499–502. https://doi.org/10.1130/G31828.1

Belousova EA, Griffin WL, O'Reilly SY, Fisher NI (2002) Apatite as an indicator mineral for mineral exploration: trace-element compositions and their relationship to host rock type. J Geochem Explore 76(1):45–69. https://doi.org/10.1016/S0375-6742(02)00204-2

Bruand E, Storey C, Fowler M (2014) Accessory mineral chemistry of high Ba–Sr granites from northern Scotland: constraints on petrogenesis and records of whole-rock signature. J Petrol 55(8):1619–1651. https://doi.org/10.1093/petrology/egu037

Bruand E, Storey C, Fowler M (2016) An apatite for progress: inclusions in zircon and titanite constrain petrogenesis and provenance. Geology 44(2):91–94. https://doi.org/10.1130/G37301.1

Cai BJ (1980) The relationship of gypsum salt beds with endogenic copper and iron ores in the Middle-Lower Yangtze Valley. Geochemica 9:193–199 (**in Chinese with English abstract**)

Cao MJ, Evans NJ, Hollings P, Cooke DR, McInnes BIA, Qin KZ (2021) Apatite texture, composition, and O-Sr-Nd isotope signatures record magmatic and hydrothermal fluid characteristics at the Black Mountain porphyry deposit, Philippines. Econ Geol 116(5):1189–1207. https://doi.org/10.5382/econgeo.4827

Cao K, Yang ZM, White NC, Hou ZQ (2022) Generation of the giant porphyry Cu–Au deposit by repeated recharge of mafic magmas at Pulang in Eastern Tibet. Econ Geol 117(1):57–90. https://doi.org/10.5382/econgeo.4860

Chelle-Michou C, Chiaradia M (2017) Amphibole and apatite insights into the evolution and mass balance of Cl and S in magmas associated with porphyry copper deposits. Contrib Mineral Petrol 172(11–12):105. https://doi.org/10.1007/s00410-017-1417-2

Chen L, Zhang Y (2018) In situ major-, trace-elements and Sr-Nd isotopic compositions of apatite from the Luming porphyry Mo deposit, NE China: constraints on the petrogenetic–metallogenic features. Ore Geol Rev 94:93–103. https://doi.org/10.1016/j.oregeorev.2018.01.026

Chu GB, Chen HY, Falloon TJ, Han JS, Zhang ST, Cheng JM, Zhang XB (2020) Early Cretaceous mantle upwelling and melting of juvenile lower crust in the Middle-Lower Yangtze River Metallogenic Belt: example from Tongshankou Cu-(MoW) ore deposit. Gondwana Res 83:183–200. https://doi.org/10.1016/j.gr.2020.02.004

Defant MJ, Drummond MS (1990) Derivation of some modern arc magmas by melting of young subducted lithosphere. Nature 347(6294):662–665. https://doi.org/10.1038/347662a0

Deng XD, Li JW, Zhou MF, Zhao XF, Yan DR (2015) In-situ LA-ICPMS trace elements and U-Pb analysis of titanite from the Mesozoic Ruanjiawan W–Cu–Mo skarn deposit, Daye district, China. Ore Geol Rev 65:990–1004. https://doi.org/10.1016/j.oregeorev.2014.08.011

Dingwell DB, Scarfe CM, Cronin DJ (1985) The effect of fluorine on viscosities in the system Na_2O–Al_2O_3–SiO_2: implications for phonolites, trachytes and rhyolites. Am Mineral 70(1–2):80–87

Duan DF, Jiang SY (2018) Using apatite to discriminate synchronous ore-associated and barren granitoid rocks: a case study from the Edong metallogenic district, South China. Lithos 310:369–380. https://doi.org/10.1016/j.lithos.2018.04.022

Duan DF, Jiang SY, Tang YJ, Wu Y, Zhou B, Zhu J (2021) Chlorine and sulfur evolution in magmatic rocks: a record from amphibole and apatite in the Tonglushan Cu–Fe (Au) skarn deposit in Hubei Province, South China. Ore Geol Rev. https://doi.org/10.1016/j.oregeorev.2021.104312

Giordano D, Romano C, Dingwell DB, Poe B, Behrens H (2004) The combined effects of water and fluorine on the viscosity of silicic magmas. Geochim Cosmochim Acta 68(24):5159–5168. https://doi.org/10.1016/j.gca.2004.08.012

Han JS, Chen HY, Hong W, Hollings P, Chu GB, Zhang L, Sun SQ (2020) Texture and geochemistry of multi-stage hydrothermal scheelite in the Tongshankou porphyry-skarn Cu–Mo (–W) deposit, eastern China: implications for ore-forming process and fluid metasomatism. Am Mineral 105(6):945–954. https://doi.org/10.2138/am-2020-7194

Holland HD (1972) The geologic history of sea water—an attempt to solve the problem. Geochim Cosmochim Acta 36(6):637–651. https://doi.org/10.1016/0016-7037(72)90108-1

Holloway JR (1976) Fluids in the evolution of granitic magmas: consequences of finite CO_2 solubility. Geol Soc Am Bull 87(10):1513–1518. https://doi.org/10.1130/0016-7606(1976)87%3c1513:FITEOG%3e2.0.CO;2

Hu H, Li JW, McFarlane CRM (2017) Hydrothermal titanite from the Chengchao iron skarn deposit: temporal constraints on iron mineralization, and its potential as a reference material for titanite U–Pb dating. Miner Petrol 111(4):593–608. https://doi.org/10.1007/s00710-017-0517-z

Hu H, Li JW, Harlov DE, Lentz DR, McFarlane CR, Yang YH (2020) A genetic link between iron oxide-apatite and iron skarn mineralization in the Jinniu volcanic basin, Daye district, eastern China: evidence from magnetite geochemistry and multi-mineral U-Pb geochronology. Geol Soc Am Bull 132(5–6):899–917. https://doi.org/10.1130/B35180.1

Keppler H (1993) Influence of fluorine on the enrichment of high field strength trace elements in granitic rocks. Contrib Mineral Petrol 114(4):479–488. https://doi.org/10.1007/BF00321752

Ketcham RA (2015) Calculation of stoichiometry from EMP data for apatite and other phases with mixing on monovalent anion sites. Am Mineral 100(7):1620–1623. https://doi.org/10.2138/am-2015-5171

Konecke BA, Fiege A, Simon AC, Parat F, Stechern A (2017) Co-variability of S^{6+}, S^{4+}, and S^{2-} in apatite as a function of oxidation state: implications for a new oxybarometer. Am Mineral 102(3):548–557. https://doi.org/10.2138/am-2017-5907

Lan TG, Hu RZ, Chen YH, Wang H, Tang YW, Liu L (2019) Generation of high-Mg diorites and associated iron mineralization within an intracontinental setting: insights from ore-barren and ore-bearing intrusions in the eastern North China Craton. Gondwana Res 72:97–119. https://doi.org/10.1016/j.gr.2019.03.008

Li WR, Costa F (2020) A thermodynamic model for F–Cl–OH partitioning between silicate melts and apatite including non-ideal mixing with application to constraining melt volatile budgets. Geochim Cosmochim Acta 269:203–222. https://doi.org/10.1016/j.gca.2019.10.035

Li JW, Zhao XF, Zhou MF, Vasconcelos P, Ma CQ, Deng XD, Souza ZSD, Zhao YX, Wu G (2008) Origin of the Tongshankou porphyry-skarn Cu–Mo deposit, eastern Yangtze craton, Eastern China: geochronological, geochemical, and Sr–Nd–Hf isotopic constraints. Miner Deposita 43(3):315–336. https://doi.org/10.1007/s00126-007-0161-3

Li JW, Zhao XF, Zhou MF, Ma CQ, Souza ZSD, Vasconcelos P (2009) Late Mesozoic magmatism from the Daye region, eastern China: U-Pb ages, petrogenesis, and geodynamic implications. Contrib Mineral Petrol 157(3):383–409. https://doi.org/10.1007/s00410-008-0341-x

Li JW, Deng XD, Zhou MF, Liu YS, Zhao XF, Guo JL (2010a) Laser ablation ICP-MS titanite U–Th–Pb dating of hydrothermal ore deposits: a case study of the Tonglushan Cu–Fe–Au skarn deposit, SE Hubei province. China Chem Geol 270(1–4):56–67. https://doi.org/10.1016/j.chemgeo.2009.11.005

Li XH, LiWX WXC, Li QL, Liu Y, Tang GQ, Gao YY, Wu FY (2010b) SIMS U–Pb zircon geochronology of porphyry Cu–Au–(Mo) deposits in the Yangtze River Metallogenic Belt, eastern China: magmatic response to early Cretaceous lithospheric extension. Lithos 119:427–438. https://doi.org/10.1016/j.lithos.2010.07.018

Li XH, Li ZX, Li WX, Wang XC, Gao Y (2013a) Revisiting the "C-type adakites" of the Lower Yangtze River Belt, central eastern China: in-situ zircon Hf–O isotope and geochemical constraints. Chem Geol 345(1):1–15. https://doi.org/10.1016/j.chemgeo.2013.02.024

Li YH, Xie GQ, Duan C, Han D, Wang CL (2013b) Effect of sulfate evaporate salt layer over the formation of skarn-type iron ore. Acta Geol Sin 87:1324–1334 (**in Chinese with English abstract**)

Li JW, Vasconcelos PM, Zhou MF, Deng XD, Cohen B, Bi SJ, Zhao XF, Selby D (2014a) Longevity of magmatic–hydrothermal systems in the Daye Cu–Fe–Au District, eastern China with implications for mineral exploration. Ore Geol Rev 57(1):375–392. https://doi.org/10.1016/j.oregeorev.2013.08.002

Li P, Zhou XH, Li ZL, Zhang AY, Zhu AA (2014b) Sedimentary characteristics and genetic analysis of worm-like limestone of Early Triassic Daye Formation in western Hubei province. Resour Environ Eng S1:31–34 (**in Chinese with English abstract**)

Li WT, Audétat A, Zhang J (2015) The role of evaporites in the formation of magnetite–apatite deposits along the Middle and Lower Yangtze River, China: evidence from LA–ICP–MS analysis of fluid inclusions. Ore Geol Rev 67:264–278. https://doi.org/10.1016/j.oregeorev.2014.12.003

Li W, Xie GQ, Mao JW, Zhu QQ, Zheng JH (2019) Mineralogy, fluid inclusion, and stable isotope studies of the Chengchao deposit, Hubei province, eastern China: implications for the formation of high-grade Fe skarn deposits. Econ Geol 114:325–352. https://doi.org/10.5382/econgeo.2019.4633

Liu YS, Hu ZC, Gao S, Günther D, Xu J, Gao CG, Chen H (2008) In situ analysis of major and trace elements of anhydrous minerals by LA-ICP-MS without applying an internal standard. Chem Geol 257:34–43. https://doi.org/10.1016/j.chemgeo.2008.08.004

Liu HB, Jin GS, Li JJ, Han J, Zhang JF, Zhang J, Zhong FW, Guo DQ (2013) Determination of stable isotope composition in uranium geological samples. World Nucl Geosci 3:174–179 (**in Chinese with English abstract**)

Lu YJ, Loucks RR, Fiorentini M, McCuaig TC, Evans NJ, Yang ZM, Hou ZQ, Kirkland CL, Parra-Avila LA, Kobussen A (2016) Zircon compositions as a pathfinder for porphyry Cu ± Mo ± Au deposits. Soc Econ Geol Special Publ 19:329–347

Manning DAC (1981) The effect of fluorine on liquidus phase relationships in the system Qz–Ab–Or with excess water at 1 kb. Contrib Mineral Petrol 76(2):206–215. https://doi.org/10.1007/BF00371960

Mao M, Rukhlov AS, Rowins SM, Spence J, Coogan LA (2016) Apatite trace element compositions: a robust new tool for mineral exploration. Econ Geol 111(5):1187–1222. https://doi.org/10.2113/econgeo.111.5.1187

McDonough WF, Sun SS (1995) The composition of the Earth. Chem Geol 120(3–4):223–253. https://doi.org/10.1016/0009-2541(94)00140-4

Meinert LD, Dipple GM, Nicolescu S (2005) World skarn deposits. Economic geology 100th anniversary volume, pp 299–336.

Nathwani CL, Loader MA, Wilkinson JJ, Buret Y, Sievwright RH, Hollings P (2020) Multi-stage arc magma evolution recorded by apatite in volcanic rocks. Geology 48(4):323–327. https://doi.org/10.1130/G46998.1

Pan LC, Hu RZ, Wang XS, Bi XW, Zhu JJ, Li CS (2016) Apatite trace element and halogen compositions as petrogenetic–metallogenic indicators: examples from four granite plutons in the Sanjiang region, SW China. Lithos 254:118–130. https://doi.org/10.1016/j.lithos.2016.03.010

Parat F, Holtz F (2004) Sulfur partitioning between apatite and melt and effect of sulfur on apatite solubility at oxidizing conditions. Contrib Mineral Petrol 147(2):201–212. https://doi.org/10.1007/s00410-004-0553-7

Parat F, Holtz F, Klügel A (2011) S-rich apatite-hosted glass inclusions in xenoliths from La Palma: constraints on the volatile partitioning in evolved alkaline magmas. Contrib Mineral Petrol 162(3):463–478. https://doi.org/10.1007/s00410-011-0606-7

Peng G, Luhr JE, McGee JJ (1997) Factors controlling sulfur concentrations in volcanic apatite. Am Mineral 82(11–12):1210–1224. https://doi.org/10.2138/am-1997-11-1217

Prowatke S, Klemme S (2006) Trace element partitioning between apatite and silicate melts. Geochim Cosmochim Acta 70(17):4513–4527. https://doi.org/10.1016/j.gca.2006.07.016

Richards JP (2011) High Sr/Y arc magmas and porphyry Cu±Mo±Au deposits: just add water. Econ Geol 106:1075–1081. https://doi.org/10.2113/econgeo.106.7.1075

Richards JP, Kerrich R (2007) Adakite-like rocks: their diverse origins and questionable role in metallogenesis. Econ Geol 102:537–576. https://doi.org/10.2113/gsecongeo.102.4.537

Rouse RC, Dunn PJ (1982) A contribution to the crystal chemistry of ellestadite and the silicate sulfate apatites. Am Mineral 67(1–2):90–96

Scholten L, Schmidt C, Lecumberri-Sanchez P, Newville M, Lanzirotti A, Sirbescu MLC, Steele-MacInnis M (2019) Solubility and speciation of iron in hydrothermal fluids. Geochim Cosmochim Acta 252:126–143. https://doi.org/10.1016/j.gca.2019.03.001

Sha LK, Chappell BW (1999) Apatite chemical composition, determined by electron microprobe and laser-ablation inductively coupled plasma mass spectrometry, as a probe into granite petrogenesis. Geochim Cosmochim Acta 63(22):3861–3881. https://doi.org/10.1016/S0016-7037(99)00210-0

Shu QA, Chen PL, Cheng JR (1992) Geology of iron-copper deposits in Eastern Hubei province. Metallurgic Industry Press, Beijing (**in Chinese**)

Simon AC, Pettke T, Candela PA, Piccoli PM, Heinrich CA (2004) Magnetite solubility and iron transport in magmatic-hydrothermal environments. Geochim Cosmochim Acta 68:4905–4914. https://doi.org/10.1016/j.gca.2004.05.033

Song HJ, Wignall PB, Tong JN, Song HY, Chen J, Chu DL, Tian L, Luo M, Zong KQ, Chen YL, Lai XL, Zhang KX, Wang HM (2015) Integrated Sr isotope variations and global environmental changes through the Late Permian to early Late Triassic. Earth Planet Sci Lett 424:140–147. https://doi.org/10.1016/j.epsl.2015.05.035

Stock MJ, Humphreys MCS, Smith VC, Johnson RD, Pyle DM (2015) New constraints on electron-beam induced halogen migration in apatite. Am Mineral 100(1):281–293. https://doi.org/10.2138/am-2015-4949

Streck MJ, Dilles JH (1998) Sulfur evolution of oxidized arc magmas as recorded in apatite from a porphyry copper batholith. Geology 26:523–526. https://doi.org/10.1130/0091-7613(1998)026%3c0523:SEOOAM%3e2.3.CO;2

Sun SJ, Yang XY, Wang GJ, SunWD ZH, Li CY, Ding X (2019) In situ elemental and Sr-O isotopic studies on apatite from the Xu-Huai intrusion at the southern margin of the North China Craton: implications for petrogenesis and metallogeny. Chem Geol 510:200–214. https://doi.org/10.1016/j.chemgeo.2019.02.010

Sun JF, Yang JH, Zhang JH, Yang YH, Zhu YS (2021) Apatite geochemical and Sr–Nd isotopic insights into granitoid petrogenesis. Chem Geol 566:120104. https://doi.org/10.1016/j.chemgeo.2021.120104

Wallace PJ (2005) Volatiles in subduction zone magmas: concentrations and fluxes based on melt inclusion and volcanic gas data. J Volcanol Geotherm Res 140:217–240. https://doi.org/10.1016/j.jvolgeores.2004.07.023

Wang LX, Ma CQ, Zhang C, Zhu YX, Marks MAW (2018) Halogen geochemistry of I- and A-type granites from Jiuhuashan region (South China): insights into the elevated fluorine in A-type granite. Chem Geol 478:164–182. https://doi.org/10.1016/j.chemgeo.2017.09.033

Webster JD, Tappen CM, Mandeville CW (2009) Partitioning behavior of chlorine and fluorine in the system apatite-melt-fluid. II: felsic silicate systems at 200 MPa. Geochim Cosmochim Acta 73(3):559–581. https://doi.org/10.1016/j.gca.2008.10.034

Wen G, Bi SJ, Li JW (2017) Role of evaporitic sulfates in iron skarn mineralization: a fluid inclusion and sulfur isotope study from the Xishimen deposit, Handan-Xingtai district, North China Craton. Miner Deposita 52:495–514. https://doi.org/10.1007/s00126-016-0674-8

Wen G, Zhou RJ, Li JW, Chang J, Hu H, Yan DR, Wei KT, Jin SG (2020a) Skarn metallogeny through zircon record: an example from the Daye Cu–Au–Fe–Mo district, eastern China. Lithos 378:105807. https://doi.org/10.1016/j.lithos.2020.105807

Wen G, Li JW, Hofstra AH, König AE, Cui B (2020b) Textures and compositions of clinopyroxene in an Fe skarn with implications for ore-fluid evolution and mineral-fluid REE partitioning. Geochim Cosmochim Acta 290:104–123. https://doi.org/10.1016/j.gca.2020.08.020

Xiao B, Pan YM, Song H, Song WL, Zhang Y, Chen HY (2021) Hydrothermal alteration processes of fluorapatite and implications for REE remobilization and mineralization. Contrib Mineral Petrol 176(10):1–12. https://doi.org/10.1007/s00410-021-01849-7

Xie GQ, Mao JW, Li RL, Qv WJ, Pirajno F, Du AD (2007) Re–Os molybdenite and Ar–Ar phlogopite dating of Cu–Fe–Au–Mo (W) deposits in southeastern Hubei, China. Mineral Petrol 90:249–270. https://doi.org/10.1007/s00710-006-0176-y

Xie GQ, Mao JW, Li LR, Bierlein F (2008) Geochemistry and Nd–Sr isotopic studies of Late Mesozoic granitoids in the southeastern Hubei province, Middle-Lower Yangtze River belt, Eastern China: petrogenesis and tectonic setting. Lithos 104:216–230. https://doi.org/10.1016/j.lithos.2007.12.008

Xie GQ, Mao JW, Li XW, Duan C, Yao L (2011a) Late Mesozoic bimodal volcanic rocks in the Jinniu basin, Middle-Lower Yangtze River Belt (YRB), East China: age, petrogenesis and tectonic implications. Lithos 127:144–164. https://doi.org/10.1016/j.lithos.2011.08.012

Xie GQ, Mao JW, Zhao HJ (2011b) Zircon U–Pb geochronological and Hf isotopic constraints on petrogenesis of Late Mesozoic intrusions in the southeast Hubei province, Middle-Lower Yangtze River belt (MLYRB), East China. Lithos 125:693–710. https://doi.org/10.1016/j.lithos.2011.04.001

Xie GQ, Mao JW, Zhao HJ, Duan C, Yao L (2012) Zircon U–Pb and phlogopite ^{40}Ar–^{39}Ar age of the Chengchao and Jinshandian skarn Fe deposits, Southeast Hubei, Middle-Lower Yangtze River Valley metallogenic belt, China. Miner Deposita 47:633–652. https://doi.org/10.1007/s00126-011-0367-2

Xie GQ, Mao JW, Zhu QQ, Yao L, Li YH, Li W, Zhao HJ (2015) Geochemical constraints on Cu–Fe and Fe skarn deposits in the Edong district, Middle-Lower Yangtze River metallogenic belt, China. Ore Geol Rev 64:425–444. https://doi.org/10.1016/j.oregeorev.2014.08.005

Xie FW, Tang JX, Chen YC, Lang XH (2018) Apatite and zircon geochemistry of Jurassic porphyries in the Xiongcun district, southern Gangdese porphyry copper belt: implications for petrogenesis and mineralization. Ore Geol Rev 96:98–114. https://doi.org/10.1016/j.oregeorev.2018.04.013

Xie GQ, Mao JW, Zhu QQ, Han YX, Li W, Duan C, Ye H (2020) Mineral deposit model of Cu–Fe–Au skarn system in the edongnan region, Eastern China. Acta Geol Sin English Ed 94(6):1797–1807. https://doi.org/10.1111/1755-6724.14597

Xing K, Shu QH, Lentz D, Wang FY (2019) Zircon and apatite geochemical constraints on the formation of the Huojihe porphyry Mo deposit in the Lesser Xing'an Range. NE China Am Mineral 105(3):382–396. https://doi.org/10.2138/am-2020-7226

Xu B, Hou ZQ, Griffin WL, Lu YJ, Belousova E, Xu JF, O'Reilly SY (2021) Recycled volatiles determine fertility of porphyry deposits in collisional settings. Am Mineral 106(4):656–661. https://doi.org/10.2138/am-2021-7714

Yan DR, Deng XD, Hu H, Li JW (2012) U-Pb age and petrogenesis of the Ruanjiawan granodiorite pluton and Xiniushan granodiorite porphyry, Southeast Hubei province: implications for Cu–Mo mineralization. Acta Petrol Sin 28(10):3373–3388 (**in Chinese with English abstract**)

Yang YH, Wu FY, Yang JH, Chew DM, Xie LW, Chu ZY, Zhang YB, Huang C (2014) Sr and Nd isotopic compositions of apatite reference materials used in U–Th–Pb geochronology. Chem Geol 385:35–552. https://doi.org/10.1016/j.chemgeo.2014.07.012

Yardley BWD (2005) Metal concentrations in crustal fluids and their relationship to ore formation. Economic geology 100th anniversary volume, p 613–632. https://doi.org/10.2113/gsecongeo.100.4.613

Zeng LP, Zhao XF, Hammerli J, Spandler C (2020) Tracking fluid sources for skarn formation using scapolite geochemistry: an example from the Jinshandian iron skarn deposit, Eastern China. Miner Deposita 55:1029–1046. https://doi.org/10.1007/s00126-019-00914-3

Zhang W, Hu ZC, Liu YS (2020a) Iso-compass: new freeware software for isotopic data reduction of LA-MC-ICP-MS. J Anal at Spectrom 35(6):1087–1096. https://doi.org/10.1039/D0JA00084A

Zhang XB, Guo F, Zhang B, Zhao L, Wu YM, Wang GQ, Alemayehu M (2020b) Magmatic evolution and post-crystallization hydrothermal activity in the early Cretaceous Pingtan instrusive complex, SE China: records from apatite geochemistry. Contrib Mineral Petrol 175(35):1–18. https://doi.org/10.1007/s00410-020-1675-2

Zhang ST, Ma Q, Chen HY, Long XP, Chu GB, Zhang WF, Cheng JM, Tian J (2021) Petrogenesis of Early Cretaceous granitoids and mafic microgranular enclaves from the giant Tonglushan Cu–Au–Fe skarn orefield, Eastern China. Lithos 392:106103. https://doi.org/10.1016/j.lithos.2021.106103

Zong KQ, Klemd R, Yuan Y, He ZY, Guo JL, Shi XL, Liu YS, Hu ZC, Zhang ZM (2017) The assembly of Rodinia: The correlation of early Neoproterozoic (ca. 900 Ma) high-grade metamorphism and continental arc formation in the southern Beishan Orogen, southern Central Asian Orogenic Belt (CAOB). Precambr Res 290:32–48. https://doi.org/10.1016/j.precamres.2016.12.010